

Figure 1.

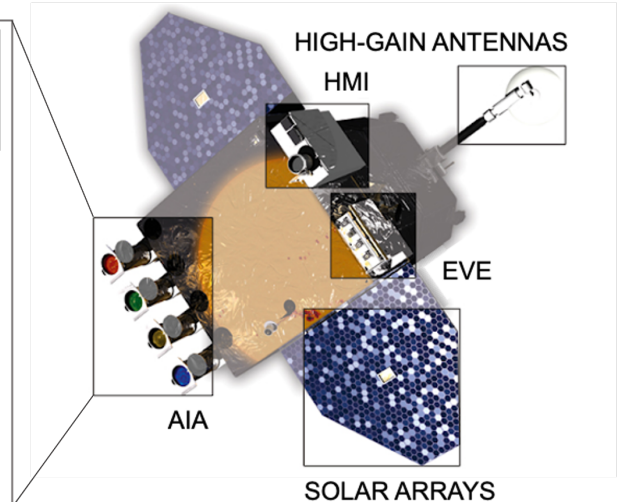
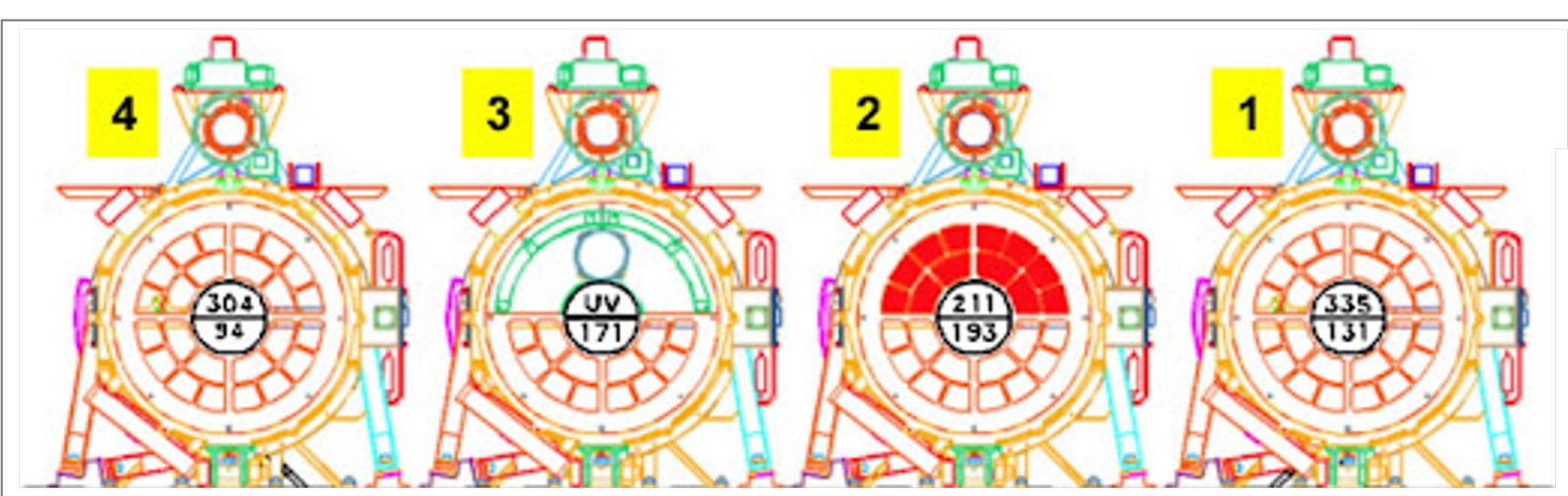


Figure 2a.



Figure 2b.

BodyX Velocity Angle (deg): 43.021
ACS Propagation Error (m): 92.040
Altitude (Re): 5.611



Earth Inertial Axes

2022181.161547 Real Time Offset: 0.00 sec

Figure 3.

Total Spikes per Image

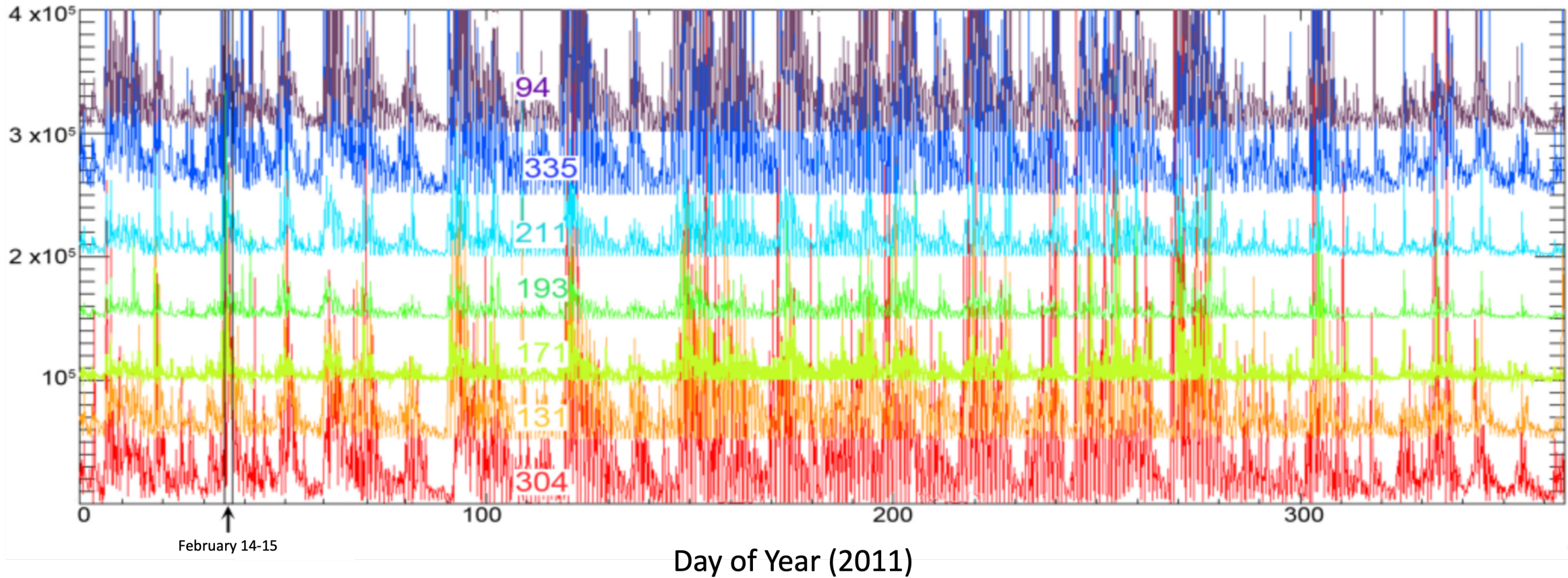
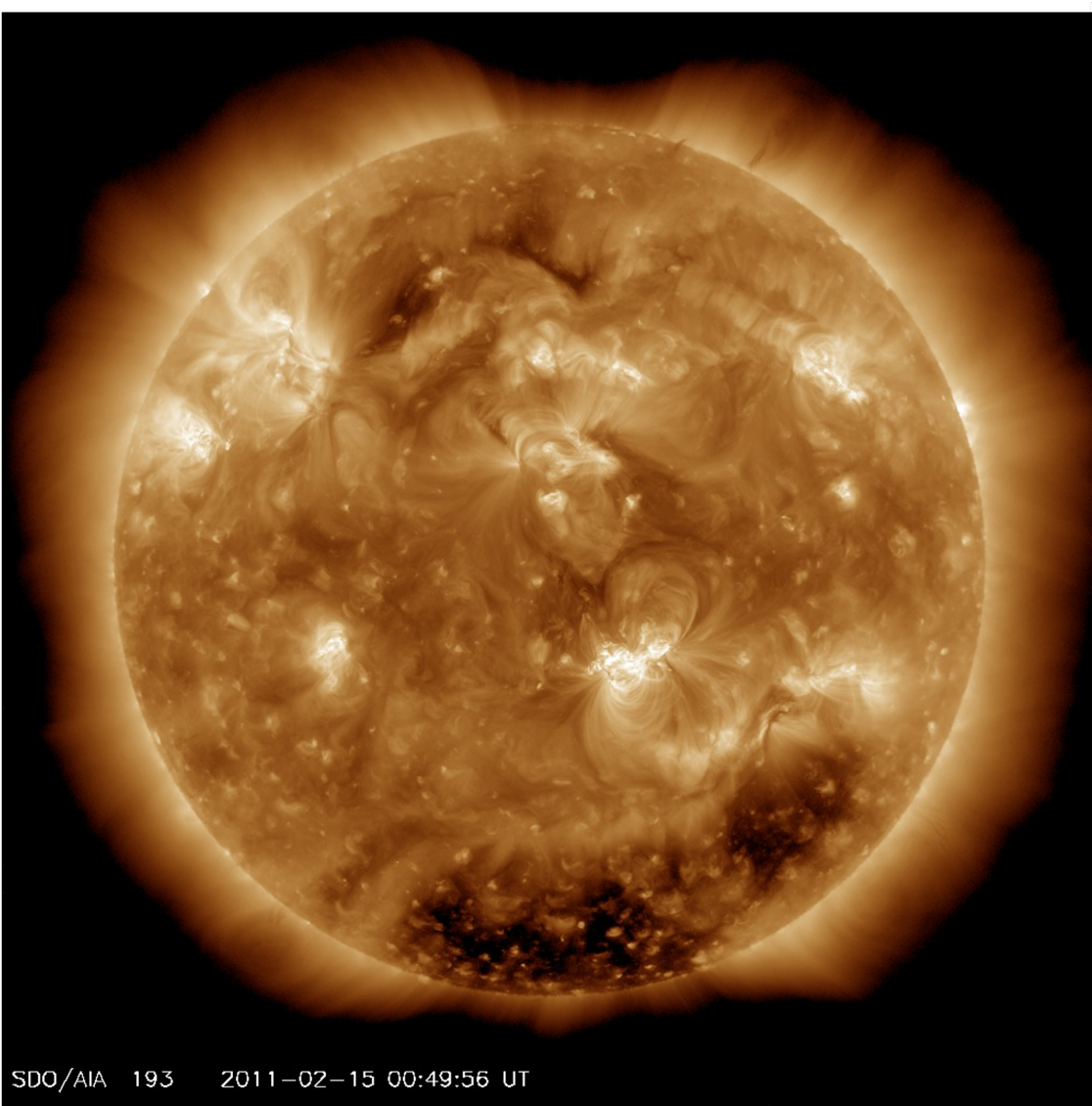


Figure 4.



SDO/AIA 193 2011-02-15 00:49:56 UT

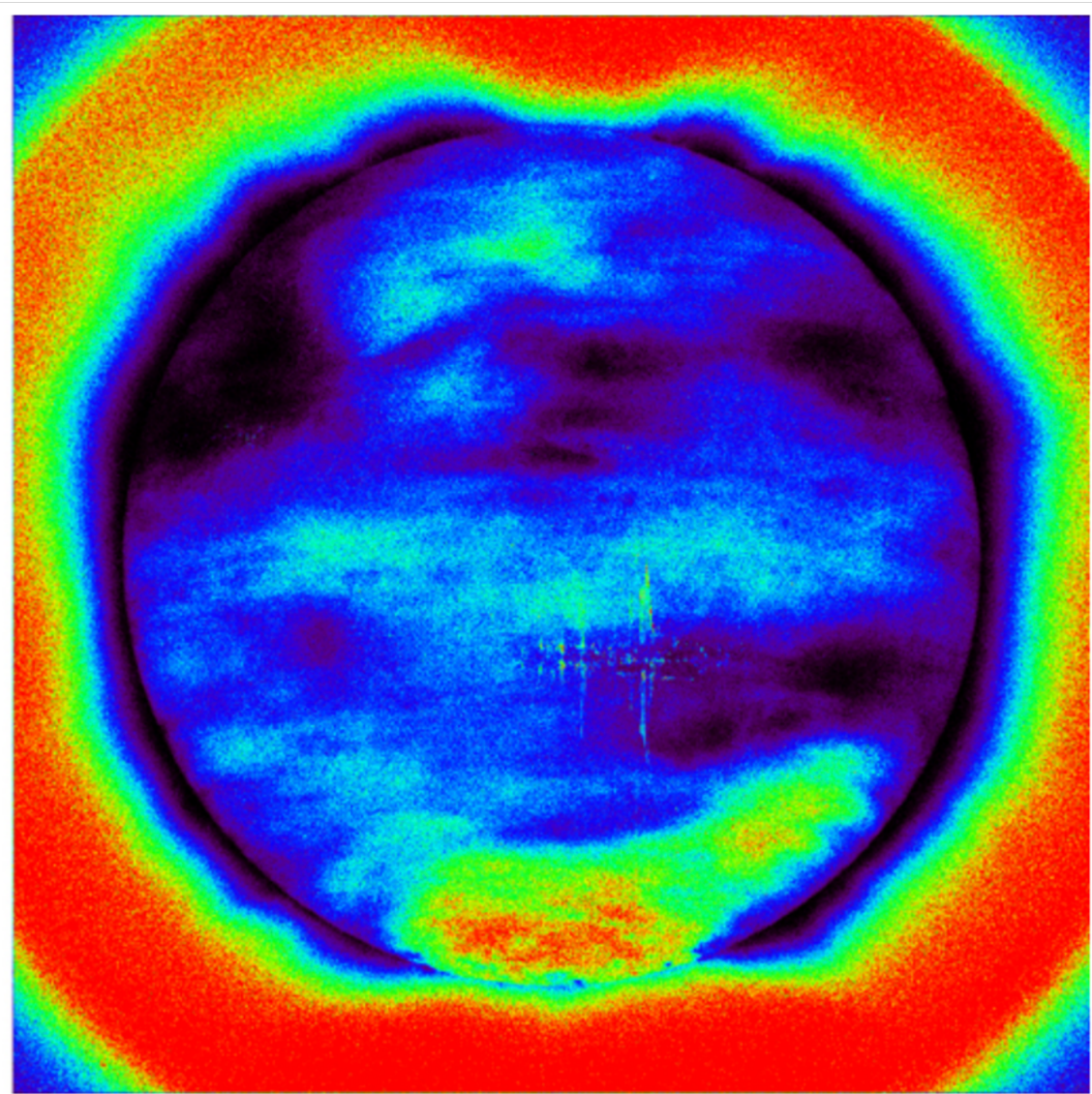


Figure 5.

Spread of NSPIKES (100 bins)

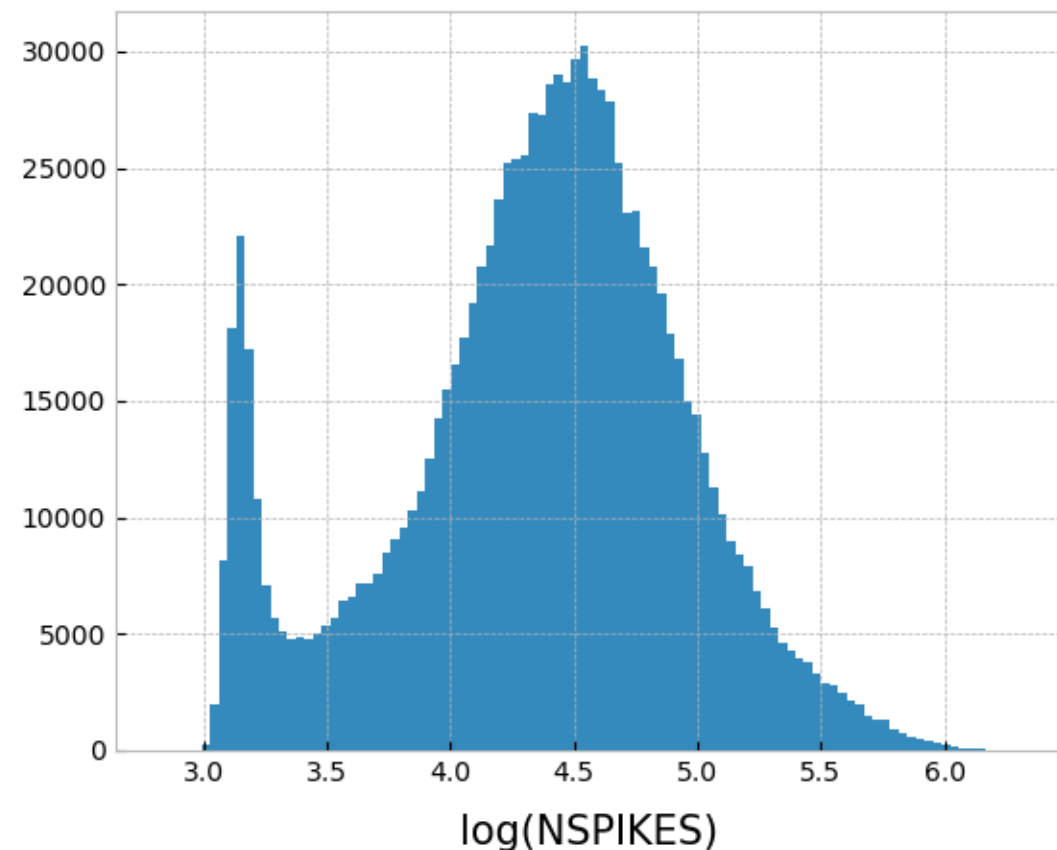
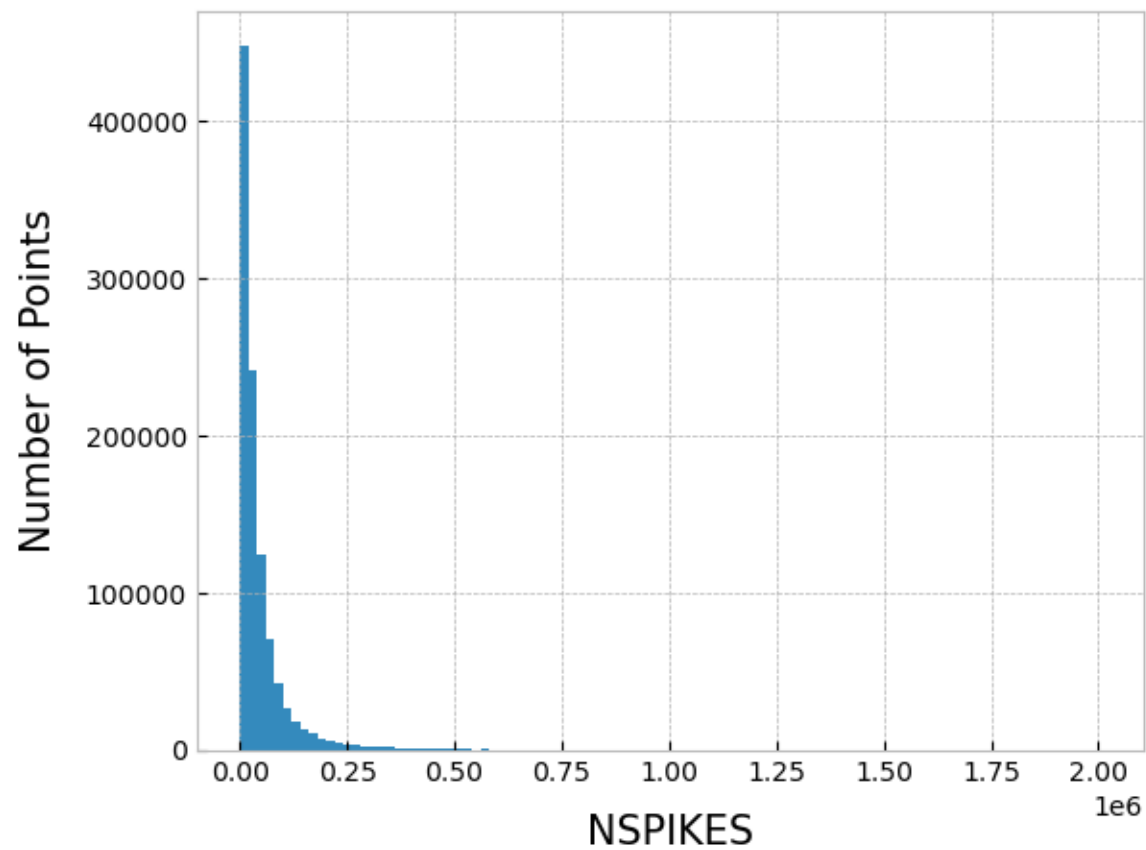


Figure 6.

Plots of NSPIKES, Kp, ap and SymH Against Time (Jan-Dec 2019)

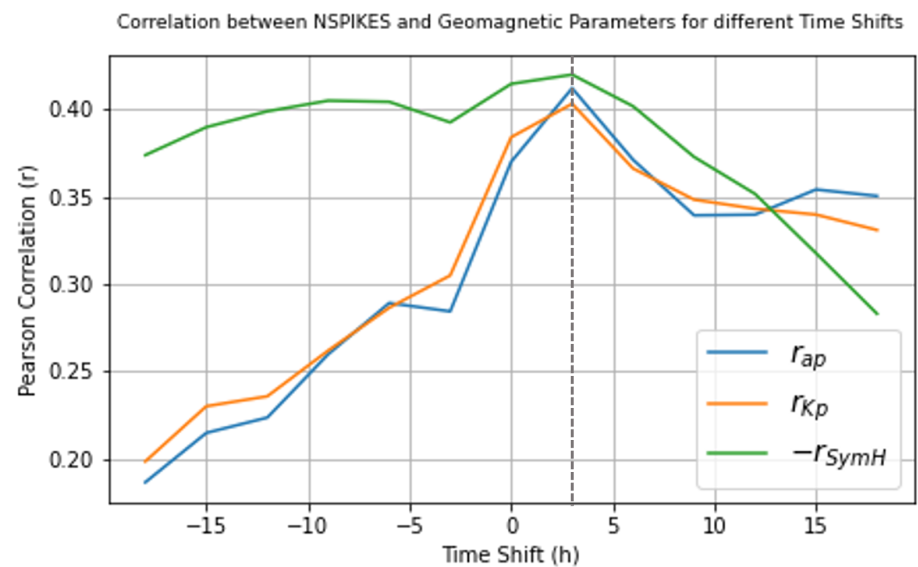
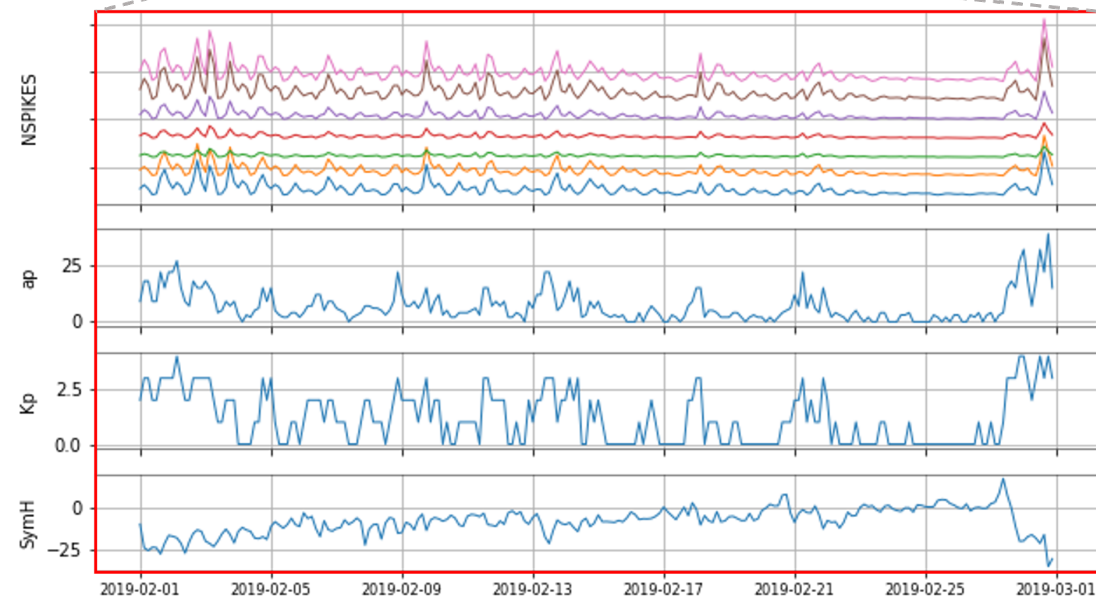
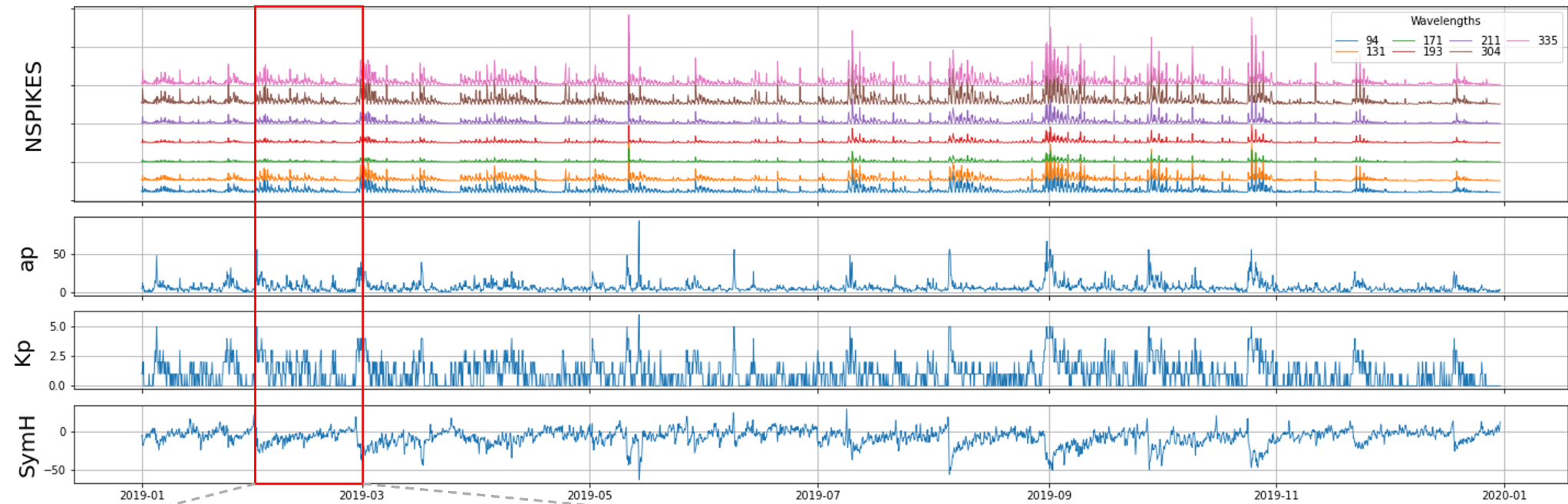
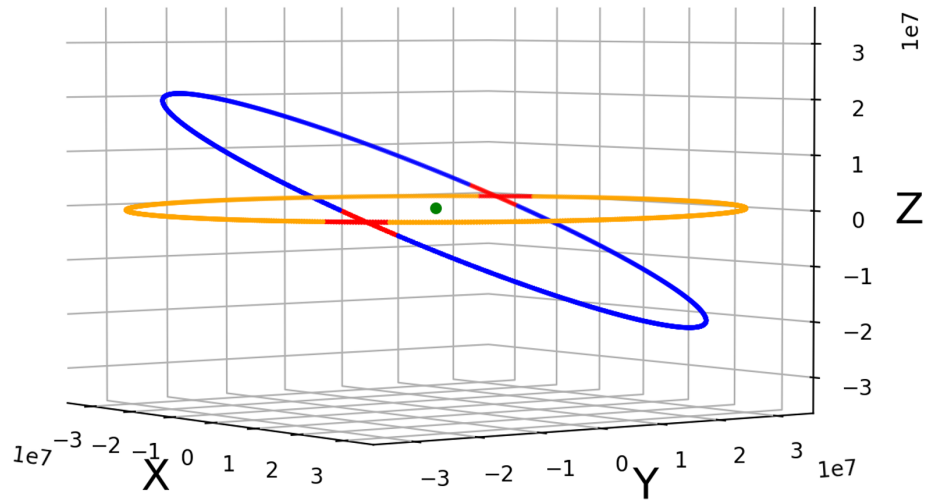
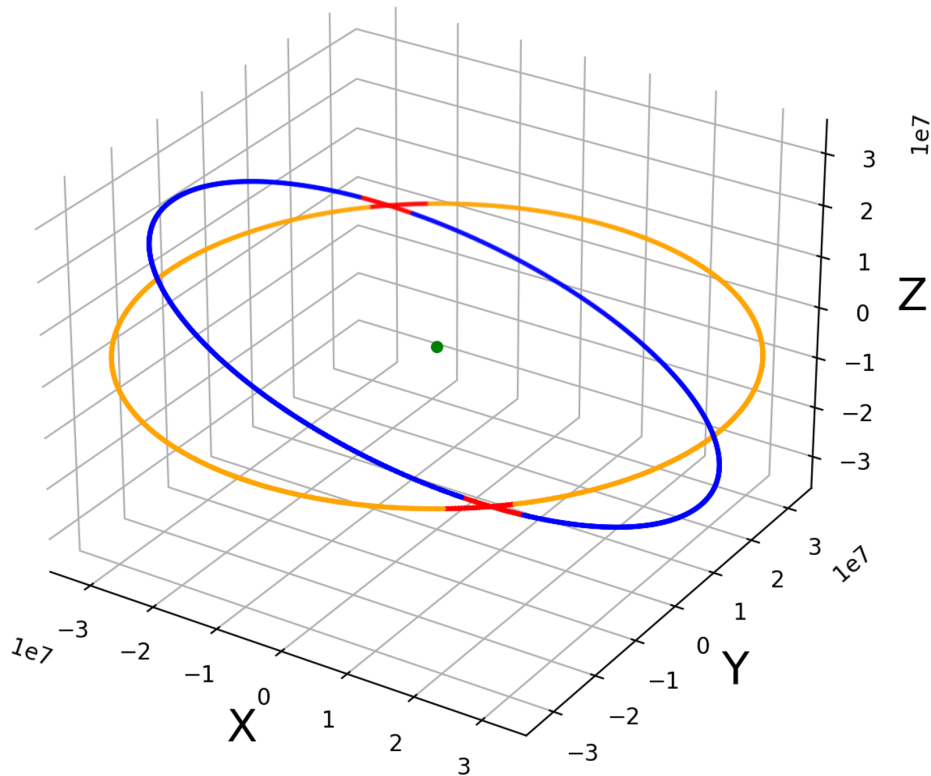


Figure 7.

SDO and GOES-14 Orbits



- SDO Orbit
- GOES-14 Orbit
- Conjunction Points
- Earth

Figure 8.

Equator Data Selection

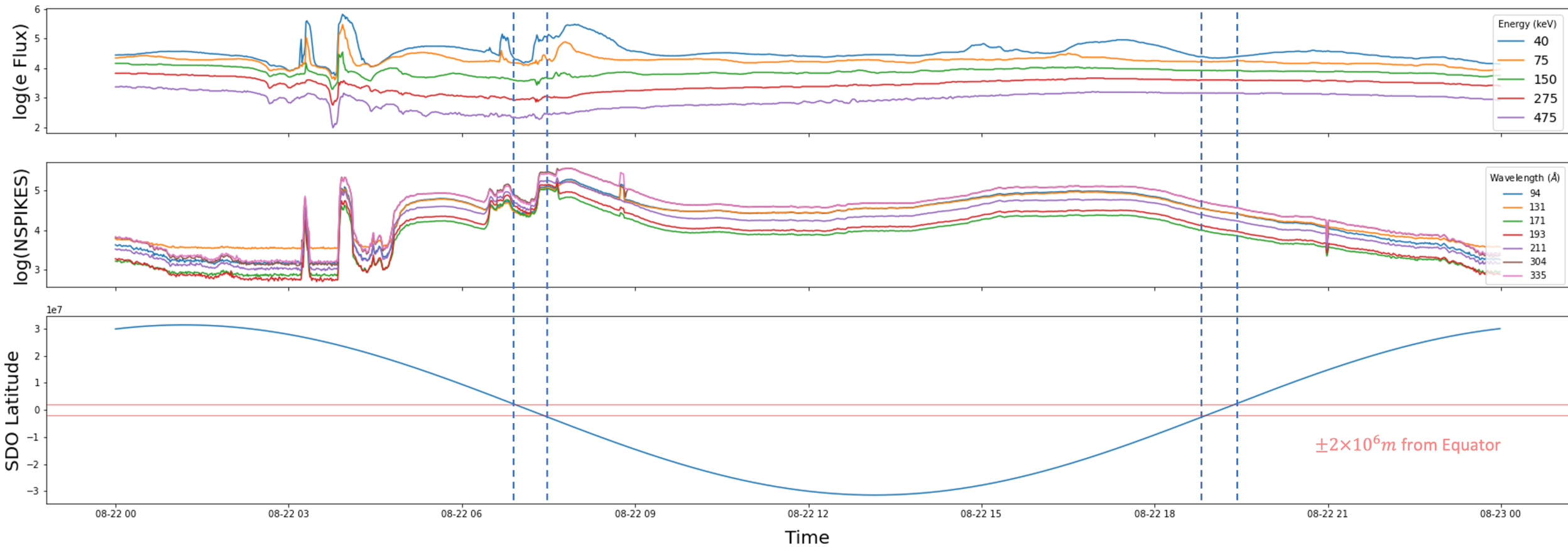


Figure 9.

SDO AIA 304Å NSPIKES vs GOES-14 MAGED Telescope 3 40keV Electrons

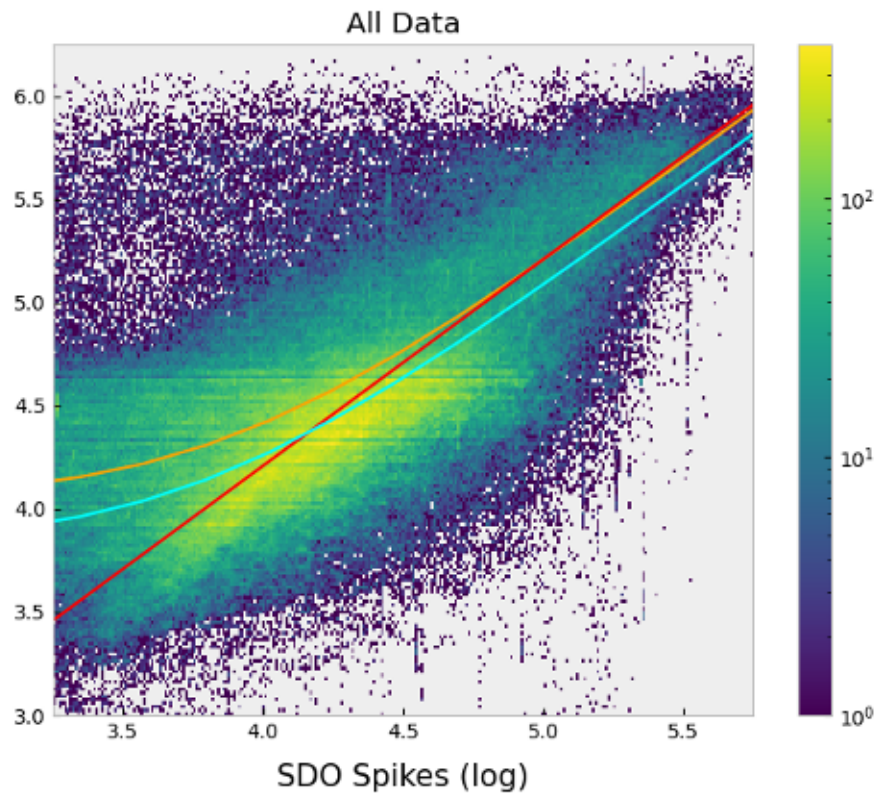
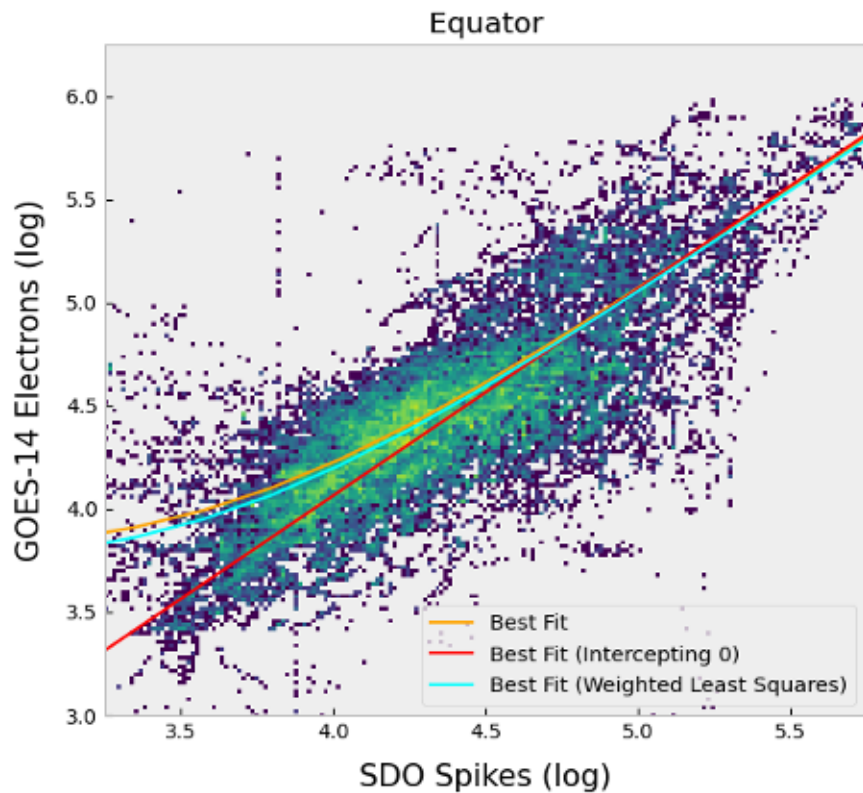
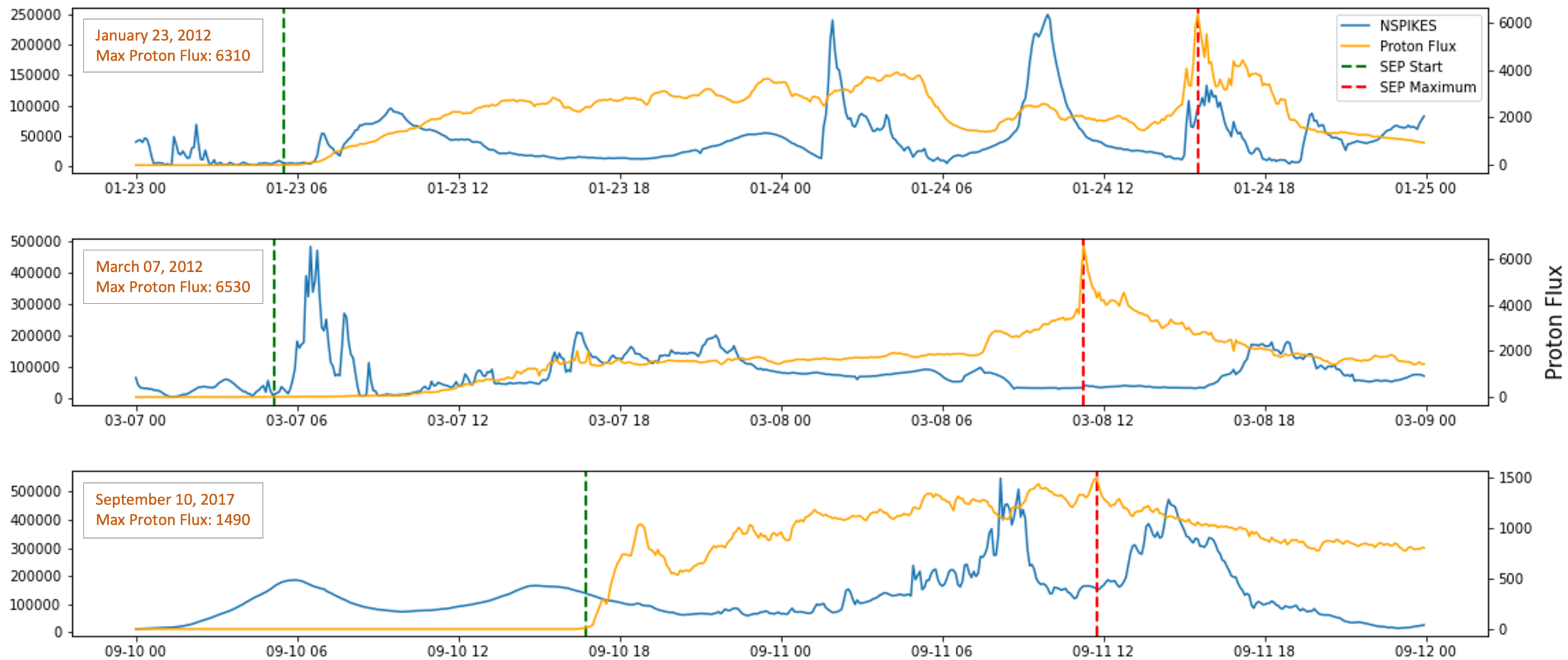


Figure 10.

NSPIKES and EPEAD Proton Flux during the 3 most intense SEP events (2010-2020)



Turning Noise into Data: Characterization of the Van Allen Radiation Belt Using SDO Spikes Data

Spiridon Kasapis^{1,2}, Barbara J. Thompson¹, Juan V. Rodriguez^{3,4}, Raphael Attie^{1,5}, Gonzalo Cucho-Padin^{6,7}, Daniel da Silva^{1,8,9}, Meng Jin¹⁰, William D. Pesnell¹

¹Solar Physics Laboratory, NASA Goddard Space Flight Center, Greenbelt, MD, USA

²Department of Climate and Space Sciences and Engineering, University of Michigan Ann Arbor, MI, USA

³Cooperative Institute for Research in Environmental Sciences, University of Colorado Boulder, CO, USA

⁴NOAA National Centers for Environmental Information, Boulder, CO, USA

⁵Physics and Astronomy Department, George Mason University, Fairfax, VA, USA

⁶Department of Physics, Catholic University of America, Washington, DC, USA

⁷Space Weather Laboratory, NASA Goddard Space Flight Center, Greenbelt, MD, USA

⁸Goddard Planetary Heliophysics Institute, University of Maryland Baltimore County, Baltimore, MD, USA

⁹Laboratory for Atmospheric and Space Physics, University of Colorado Boulder, CO, USA

¹⁰Lockheed Martin Solar and Astrophysics Laboratory, Palo Alto, CA, USA

Key Points:

- More than 3 trillion “spiked pixels” attributed to magnetospheric particle impacts have been removed from the SDO/AIA images so far.
- The SDO spike rate was compared to particle measurements from GOES-14 during close orbital conjunctions occurring twice daily over 27 months.
- High correlation between AIA spikes and GOES-14 electrons is found, therefore SDO can provide proxy measurements for radiation belt electrons.

Abstract

The Solar Dynamics Observatory (SDO) is a solar mission in an inclined geosynchronous orbit. Since commissioning, images acquired by Atmospheric Imaging Assembly (AIA) instrument on-board the SDO have frequently displayed “spikes”, pixel regions yielding extreme number of digital counts. These are theorized to occur from energetic electron collisions with the instrument detector system. These spikes are regularly removed from AIA Level 1.0 images to produce clean and reliable data. A study of historical data has found over 100 trillion spikes in the past decade. This project correlates spike detection frequency with radiation environment parameters in order to generate an augmented data product from SDO. We conduct a correlation study between SDO/AIA data and radiation belt activity within the SDO’s orbit. By extracting radiation “spike” data from the SDO/AIA images, we produce a comprehensive data product which is correlated not only with geomagnetic parameters such as Kp, Ap and Sym-H but also with the electron and proton fluxes measured by the GOES-14 satellite. As a result, we find that AIA spikes are highly correlated with the GOES-14 electrons detected by the MAGED and EPEAD instruments at the equator (where the two satellites meet) with Spearman’s Correlation values of $\rho = 0.73$ and $\rho = 0.53$ respectively, while a weaker correlation of $\rho = 0.47$ is shown with MAGPD protons for the two year period where both missions returned data uninterruptedly. This correlation proves that the SDO spike data can be proven useful for characterizing the Van Allen radiation belt, especially at areas where other satellites cannot.

Plain Language Summary

The Solar Dynamics Observatory (SDO) is a NASA mission that has been observing the Sun since 2010. One instrument aboard SDO is the Atmospheric Imaging Assembly (AIA) which acquires pictures of the Sun in seven extreme ultraviolet (EUV) and two ultraviolet (UV) channels. The AIA detector is designed to capture solar photons of different wavelengths to create images. However, SDO is located in a geosynchronous orbit, which passes through regions of the outer radiation belt. Energetic particles that impact the detector result in brightened pixels in the SDO images. An algorithm removes and records these unusual pixels in every AIA image. Although these pixels are considered noise, in this research we use them to infer the particle density along SDO’s orbit. This paper proves that the fluctuation of the number of noisy pixels in AIA’s images best matches the fluctuation of the electron readings from the nearby GOES-14 weather satellite. This research shows that these noisy pixels can be turned to a data product useful for characterizing the Van Allen radiation belt.

1 Introduction

Sometimes the proverb “one man’s trash is another man’s treasure” is also apt in science, as that which is considered noise in one scientific enquiry might be found to be insightful data in another. This has lately been observed in the field of heliophysics.

Early after its launch, the Solar Terrestrial Relations Observatory (STEREO) mission team observed that an unusually high number of spacecraft-related “debris” were being detected by its coronagraphic instruments (SECCHI suite) compared to other previously flown similar detectors. When St Cyr et al. (2009) compared the SECCHI “debris storms” with S/WAVES, they found that almost all are coincident with the most intense transient emissions observed by the radio and plasma waves instrument. They concluded that the debris came from the spacecraft thermal blanketing caused by impacts of large interplanetary dust grain storms that are detected by S/WAVES. Based on this debris-storm correlation, proxy measurements for interplanetary dust distributions could be obtained.

74 Using the Solar and Heliospheric Observatory (SOHO) data, Didkovsky et al. (2006)
75 created a tool to indirectly measure proton flux which was based on the energy deposited
76 by protons in 128×128 pixel Extreme Ultraviolet Imaging Telescope (EIT) charge-coupled
77 device (CCD) areas outside the solar disk images. This tool was tested by comparing
78 Solar Energetic Particles (SEP) flux temporal profiles extracted from the EIT CCD frames
79 and downloaded from the GOES database for a number of early 2000s events. The SEP
80 flux temporal profiles and the relatively narrow energy ranges between 45 and 440 MeV
81 EIT proton spectra reported in their work correlates well with the GOES profiles. SOHO
82 is at the Sun-Earth first Lagrange point (L1).

83 Carlton et al. (2018) suggested that his approach of using Galileo images backgrounds
84 can be applied to other sets of imaging data (star trackers) in energetic electron envi-
85 ronments, such as those found in Geostationary Earth Orbit (GEO). A similar approach
86 is followed in this paper for indirectly inferring electron fluxes within the Van Allen outer
87 radiation belt. Named after James Van Allen who first confirmed its existence using data
88 from Explorer 1, the Van Allen radiation belt was one of the first discoveries of the space
89 age (W. Li & Hudson, 2019). A number of missions (even early ones such as Explorer
90 3 and 4, Pioneer 3, and Luna 1) have been equipped with instruments which are geared
91 towards mapping the radiation belts, the most representative one being the Van Allen
92 Probes (Kurth et al., 2015).

93 To get a full picture of the Van Allen radiation belts, satellites that orbit the Earth
94 in unique ways are necessary. A good example, is the Solar Anomalous and Magneto-
95 spheric Particle Explorer (SAMPEX), which using its low-altitude polar orbit, has pro-
96 vided a unique long-term global picture of the radiation belts since its launch in 1992
97 (X. Li et al., 2001). Launched in 1966, the Applications Technology Satellite 1 (ATS-
98 1) was the first to observe charged particle fluxes in geosynchronous orbit (Lanzerotti
99 et al., 1967; Lezniak et al., 1968; G. Paulikas & Blake, 1979). NOAA has monitored solar-
100 origin and radiation belt particles in GEO since 1975 with the long series of Geostation-
101 ary Operational Environmental Satellites (GOES). In this paper we undertake the chal-
102 lenge of helping this characterization effort using data from the Solar Dynamics Obser-
103 vatory (SDO), a satellite that was not deployed to study the Van Allen radiation belts
104 nor does it carry instruments geared towards such a task. By showing that SDO's spike
105 data (otherwise treated as noise) correlate well with the radiation belt electron flux read-
106 ings of GOES-14, we prove that in the future it can be used by the space science com-
107 munity as a data product useful for real-time characterization of the radiation belts.

108 2 SDO Satellite and Orbit

109 The SDO spacecraft was developed at NASA's Goddard Space Flight Center and
110 launched on 11 February 2010 from the Cape Canaveral Space Force Station as the first
111 flagship mission of NASA's Living With a Star (LWS) program¹. Although its primary
112 mission was planned to last five years (2015), SDO is expected to remain operational un-
113 til 2030. Its primary goal is to understand those solar variations that influence life on
114 Earth and humanity's technological systems, aiming towards developing predictive ca-
115 pabilities of the solar activity. Insights gained from SDO investigations aim on giving
116 the heliophysics community a better understanding of how the Sun's magnetic field is
117 generated and structured along with how through solar wind, energetic particles and vari-
118 ations in the solar irradiance, it affects the heliosphere and geospace (Pesnell et al., 2011).

119 To do the above, other than its two solar arrays and two high-gain antennas, SDO
120 is equipped with three instruments as seen in Figure 1: a) the Extreme Ultraviolet Vari-
121 ability Experiment (EVE Woods et al. (2010)), b) the Helioseismic and Magnetic Im-

¹ <https://lws.gsfc.nasa.gov/>

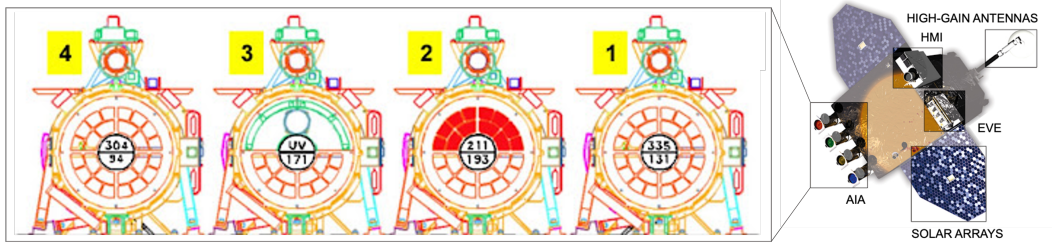
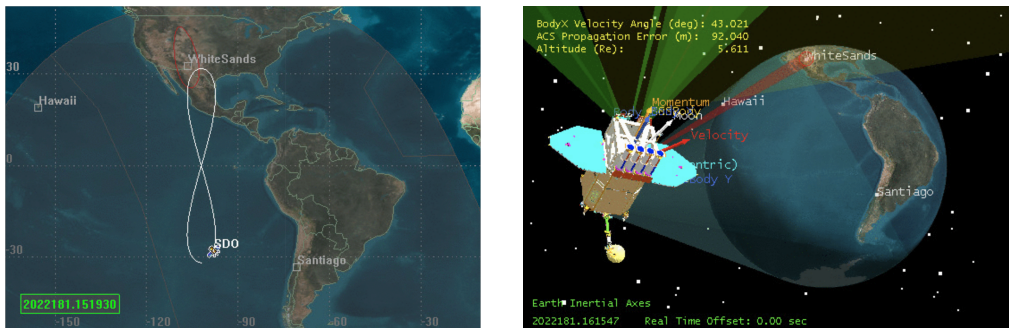


Figure 1: Artist’s impression of the SDO Satellite with its High-Gain Antennas, Solar Arrays and three scientific instruments: HMI, EVE and AIA (used in this research). The diagram on the left presents the layout of the wavelength channels or band passes in each of the four AIA telescopes (Lemen et al., 2011; Pesnell et al., 2011)

122 ager (HMI, Scherrer et al. (2012)) and c) the Atmospheric Imaging Assembly (AIA, Lemen
 123 et al. (2011)). The instruments were built in partnership with the University of Colorado
 124 Boulder’s Laboratory for Atmospheric and Space Physics (LASP²), Stanford University
 125 Hansen Experimental Physics Laboratory (HEPL³) and Lockheed Martin Solar and As-
 126 trophysics Laboratory (LMSAL⁴) respectively.

127 This research uses meta-data associated with AIA’s high-resolution full-disk im-
 128 ages of the corona and solar transition region, taken up to 0.5 solar radii (R_{\odot}) above the
 129 solar limb. The multiple images are taken from the array of four telescopes seen in Fig-
 130 ure 1 with 1.5-arcsec spatial resolution and 12-second temporal resolution. Filters on the
 131 telescopes cover ten different wavelength bands that include two ultraviolet, one visible
 132 light band and seven extreme ultraviolet (EUV) which are used in this research ($\lambda \in$
 133 $[94, 131, 171, 193, 211, 304, 335] \text{ \AA}$).



(a) The elongated figure-eight orbit as it is viewed by SDO’s ground station.

(b) SDO’s orbit allows its high-gain antenna to maintain continuous contact with NM.

Figure 2: Relying on a single site (White Sands, NM) reduces the complexity of the ground system, offering rapid cadence and continuous coverage required for the SDO science observations.

² <https://lasp.colorado.edu/>

³ <https://hepl.stanford.edu/>

⁴ <https://lmsal.com/>

134 SDO is in a circular geosynchronous orbit (6.6 Earth Radii) inclined by 28.5° which
 135 allows the spacecraft to maintain nearly continuous contact with a ground station in White
 136 Sands, New Mexico, avoiding implementation of sophisticated techniques such as com-
 137 bining data from multiple and widely spaced antennas scattered around the globe. The
 138 inclined orbit enables SDO⁵ to reduce the number of eclipses when it passes through the
 139 Earth’s night side. The SDO orbit ranges from about 32° North to 32° South in latitude
 140 and is at 108° West longitude. When viewed from the ground station, the orbit resem-
 141 bles an annalemma (elongated figure eight) as it orbits the Earth once per day. The or-
 142 bit of the SDO will be discussed again in Section 5 when compared to the orbit of GOES-
 143 14.

144 3 AIA Spike Data

145 The AIA investigation applies a “despiking” algorithm (Lemen et al., 2011) to all
 146 EUV Level-1 data in order to remove brightened pixels that result, primarily, from the
 147 local particle population at SDO’s geosynchronous location. A typical 304 \AA image, for
 148 example, contains over 50,000 “despiked” pixels (0.3% of 16 Megapixels), but the num-
 149 ber can be in the millions during periods of enhanced particle flux. Without the despik-
 150 ing algorithm, several AIA images would be unreliable for scientific purposes. The de-
 151 spiking algorithm, however, does not always distinguish between compact brightenings
 152 of solar (photon) origin and particle hits.

153 Each AIA Level-1 image has an associated “spikes.fits” file containing the removed
 154 spike data, so that a user can restore them in an image if some of the spikes were of solar
 155 origin (such as the case of the P. Young et al. (2013) flare kernels and the P. Young
 156 & Muglach (2014) coronal hole jets). However, an investigation of the compact brighten-
 157 ings by Kirk et al. (2017, 2014) showed that fewer than 0.1% of the spikes are of real
 158 solar (photon) origin (P. R. Young et al., 2021). Therefore, the “spiked pixels” observed
 159 over the course of the SDO mission so far are predominantly of magnetospheric origin,
 160 presenting a rich data resource that can be used to examine particle source populations.
 161 As there are over 200 million AIA images, this represents an extensive data set, with an
 162 estimated 6×10^{12} pixel hits over the course of twelve years of operation.

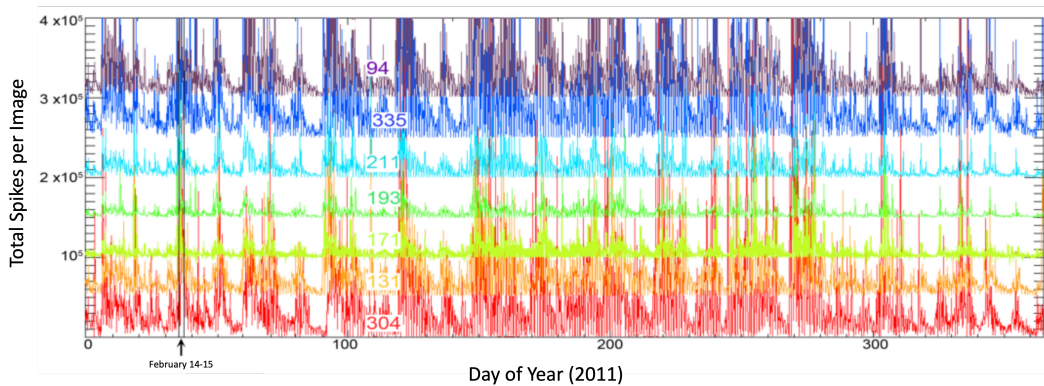


Figure 3: Number of AIA despiked pixels per 16-megapixel image for the year 2011. The 304 \AA numbers are to scale; other wavelengths are offset by multiples of 50,000 to enhance visibility. The arrow indicates the 48-hour time period seen in Figure 4.

⁵ <https://sdo.gsfc.nasa.gov/mission/moc.php>

163 Figure 3 shows the number of spiked pixels in each of the seven AIA EUV wave-
 164 lengths over the course of 2011. It is noteworthy that: 1) the number of spikes per im-
 165 age can vary greatly not only in time, but from wavelength to wavelength, and 2) while
 166 there is some correlation between enhanced periods from one day to the next, the de-
 167 gree of enhancement can vary greatly. To determine the nature of a particular spike, there
 168 are several factors at play, including the detectability of the spike against the background
 169 solar signal.

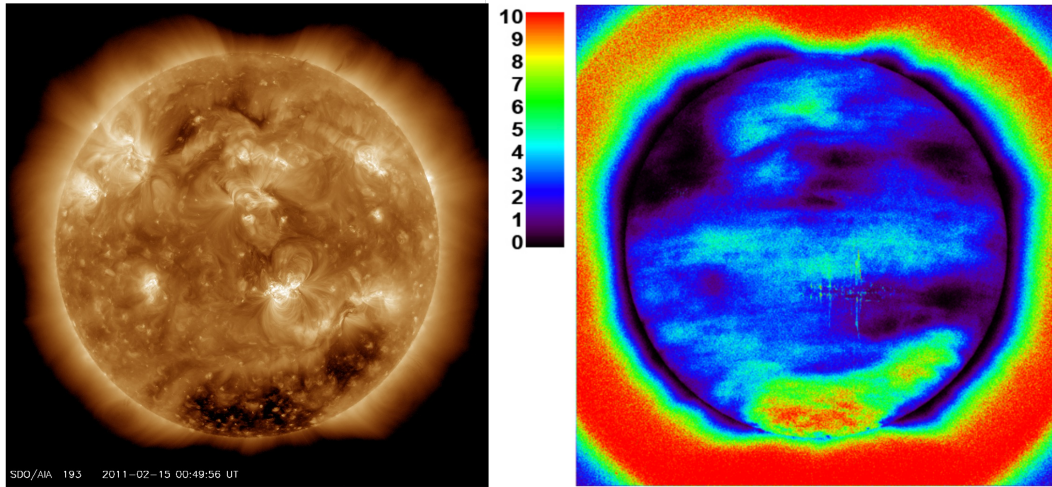


Figure 4: The left panel shows an AIA 193 Å image taken at the midpoint of the 48-hour sampling period (14th and 15th of February, 2011). The right panel shows a heatmap of all AIA 193 Å spike locations integrated over the same 48-hour period (14,383 total images). The despiking algorithm is more efficient at finding spikes in darker regions than in brighter regions.

170 Figure 4 demonstrates how a lower background signal increases the odds of spike
 171 detection. Darker regions (coronal holes and off-limb) contain the most spikes in the AIA
 172 spikes database. Since the location of magnetospheric particle hits on the detector should
 173 not correlate with solar features, the higher spike densities in dark regions are due to the
 174 AIA algorithm's likelihood of identifying a spike. Fortunately, the overwhelming major-
 175 ity of the spikes were observed off the solar limb, and the values did not fluctuate sig-
 176 nificantly with solar structure.

177 However, during periods of extremely high particle flux, there is an increased chance
 178 of coincident particle hits at the same location in two different telescopes simply due to
 179 the extra particles. Therefore, a small population of coincidental spikes that mimic multi-
 180 thermal behavior must be taken into account. AIA consists of four telescopes, and the
 181 wavebands corresponding to the outer pair (94, 131, 304 and 335 Å) show consistently
 182 higher spike levels per unit exposure time than the inner telescope wavebands (171, 193
 183 and 211 Å). Finally, the AIA wavebands have multi-thermal contributions from multi-
 184 ple spectral lines. It is for these reasons that a simplistic approach to database mining
 185 is insufficient, the AIA investigation therefore employs advanced methods to ensure that
 186 these various factors are taken into account.

187 Rather than exploring the nature of the different spikes, the present research ef-
 188 fort utilizes the outcome of the AIA investigation algorithm -the number of spikes (namely
 189 the NSPIKES header on SDO's metadata) detected in every single EUV image- as is.
 190 However, by studying the variation of NSPIKES through time and comparing it with

191 the geomagnetic indices and the particles detected by the GOES-14 instruments we can
 192 gain information about the nature of the spikes.

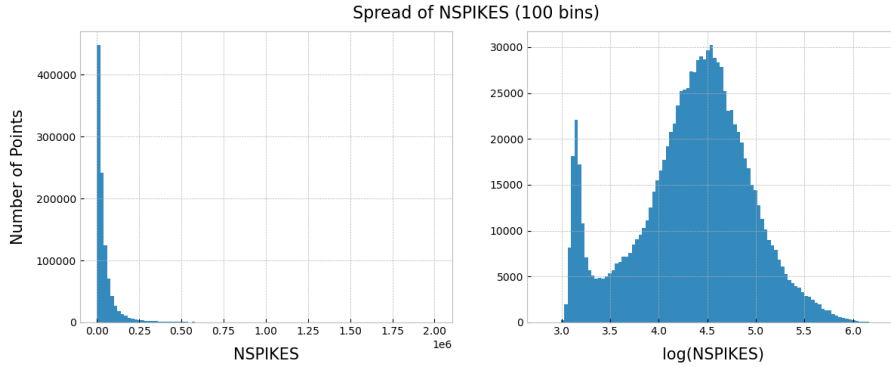


Figure 5: Histograms where the number of spikes in each AIA 304 Å image are put in 100 bins. The left histogram shows the distribution of the NSPIKES data, while the right histogram shows the distribution of the NSPIKES values in a logarithmic scale.

193 Figure 5 shows the number of spikes in a histogram distribution of a series of 100
 194 intervals (“bins”). The overwhelming majority of the NSPIKES falls into the first twelve
 195 bins with values that range from 0 to 250,000. However, in rare occasions, AIA images
 196 can contain up to 2,000,000 spikes. To deal with these outlier values, we often use the
 197 logarithm of NSPIKES which yields two Gaussian distributions (a narrower for low NSPIKES
 198 values and a wider for regular ones) of the data as seen in the right histogram. The first
 199 Gaussian distribution that appears at the logarithmic histogram is for an NSPIKES range
 200 between 1000 and 1500. We find that this lower value distribution represents spikes de-
 201 tected at the highest and lowest latitudes of the SDO orbit, therefore it represents read-
 202 ings in the magnetospheric cusp. Although this first distribution can be found useful for
 203 characterizing the open field lines of the upper and lower magnetosphere, in this study
 204 we focus on correlations within closed field regions of the magnetosphere, and only use
 205 NSPIKES values that are greater than 1500. This lower value NSPIKES distribution will
 206 be further discussed in Section 7 as it is useful material for future studies. In the next
 207 chapter we will be comparing the NSPIKES values (≥ 1500) above with a) three geo-
 208 magnetic indices and b) with the particles detected by three GOES-14 instruments.

209 4 Correlation with Geomagnetic Parameters

210 A preliminary study conducted suggests that there is some correlation between geo-
 211 magnetic parameters and the number of spikes seen in the AIA images. The geomag-
 212 netic parameters that were investigated are Sym-H and K-index (from which Kp and ap
 213 are derived).

214 Sym-H (abbreviation for symmetric disturbance of horizontal geomagnetic fields)
 215 is a proxy of the axially symmetric magnetic field disturbance at low and middle lati-
 216 tudes on the Earth’s surface measured in nano-Tesla (nT). Sym-H is an important in-
 217 dex for space weather as it indicates the intensity of a magnetic storm similarly to Dst
 218 (Wanliss & Showalter (2006)) but with a much higher time resolution (1 minute cadence).
 219 It is recorded every one minute and in our study it varies mainly from 50 (quiet) to -200
 220 (average intensity magnetic storm as discussed by Cai et al. (2009)).

221 K-index⁶ is quasi-logarithmic local index of the 3-hourly range in magnetic activ-
 222 ity relative to an assumed quiet-day curve for a single geomagnetic observatory site. Men-
 223 vielle & Berthelier (1991); Matzka et al. (2021) explain how Kp is derived from the mean
 224 standardized K-index readings from 13 geomagnetic observatories between 44 degrees
 225 and 60 degrees northern or southern geomagnetic latitude and is designed to measure
 226 solar particle radiation by its magnetic effects. The scale of Kp ranges from 0 to 9 and
 227 is expressed in thirds of a unit using a plus or minus sign for notation (e.g. 5- is 4 2/3,
 228 5 is 5 and 5+ is 5 1/3). Using Kp, a linear equivalent is derived, the ap index, which ranges
 229 from 0 to 400 and is also calculated in 3-hour intervals (Rangarajan & Lyemori (1997)).

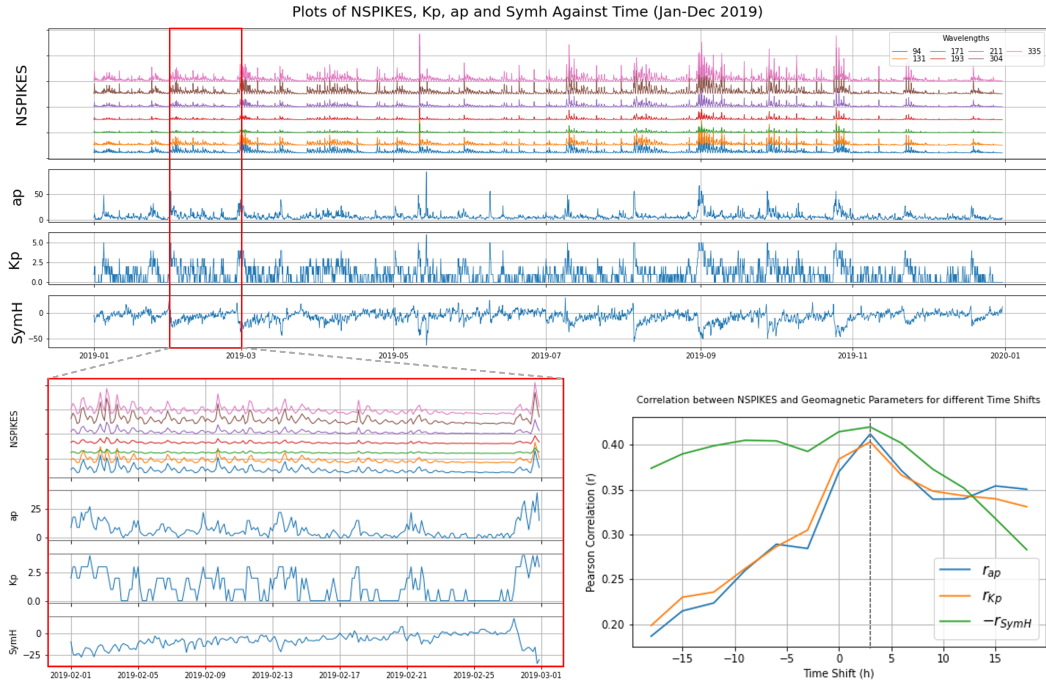


Figure 6: The top panel shows a timeline of the seven different AIA wavelength NSPIKES along with the geomagnetic parameters Sym-H, Kp and Ap for the entire year of 2019. The bottom left panel presents the timeline for the month of February 2019. The bottom right panel shows the Pearson Correlation values for different time shifts of the NSPIKES timeline.

230 To evaluate the correlation between the NSPIKES variable and the different ge-
 231 omagnetic parameters we use two different coefficients, the Pearson Correlation Coef-
 232 ficient (Pearson, 1896) and the Spearman’s Rank Correlation Coefficient (Spearman, 1961).
 233 The Pearson coefficient (r) is a measure of linear correlation between two sets of data.
 234 The r coefficient is defined as the ratio between the covariance of two variables and the
 235 product of their standard deviations. It is essentially a normalized measurement of the
 236 covariance and therefore takes values between -1 and 1. If $r > 0$ then there is positive
 237 association and if $r < 0$ there is a negative association, that is, as the value of one vari-
 238 able increases, the value of the other variable increases or decreases respectively. An $r =$
 239 0 means that there is no association between the two variables. On the other hand, the
 240 Spearman coefficient (ρ) assesses how well the relationship between two variables can

⁶ https://www.ngdc.noaa.gov/stp/GEOMAG/kp_ap.html

241 be described using a monotonic function. More specifically, ρ is equal to the Pearson cor-
 242 relation between the rank values of those two variables. Similar to r , a perfect Spear-
 243 man correlation of 1 or -1 occurs when each of the variables is a perfect monotone func-
 244 tion of the other. The Pearson and Spearman coefficients will be used throughout the
 245 paper as a measure of correlation between parameters.

246 The first plot on the top part of Figure 6 presents the number of spikes detected
 247 in all seven wavelengths of the AIA instrument against time. We plot the data for the
 248 entirety of 2019 taking 3 hour averages to match the geomagnetic parameters cadence
 249 (SDO has an 12 second cadence therefore we take the average of about 1000 SDO data
 250 points). The second, third and fourth plots on top are the ap, Kp and Sym-H index val-
 251 ues against time for the same interval, respectively. It can be easily observed that when
 252 there is an increase on the NSPIKES parameter on the top part of Figure 6, the geomag-
 253 netic parameters Kp and ap increase while Sym-H decreases. The correlation between
 254 NSPIKES and the geomagnetic parameters is even more evident when looking into a sin-
 255 gle month. On the bottom left part of Figure 6 a comparison of the number of spikes
 256 with the geomagnetic parameters is performed for the second month (February) of 2019.
 257 Similarly, it is observed that an increase of Kp and ap (or decrease for Sym-H) is followed
 258 by a corresponding increase in the number of spikes. The increased spikes values at the
 259 beginning and the end of the month are a representative example. Indicative of this re-
 260 lationship are the values of the Pearson and Spearman coefficients calculated. For the
 261 month of February 2019, NSPIKES (335 Å) yields an $r = 0.52$ and a $\rho = 0.53$ when
 262 compared against Kp, an $r = 0.50$ and a $\rho = 0.53$ when compared against ap while
 263 an $r = -0.46$ and a $\rho = -0.46$ when compared against Sym-H (negative correlation).
 264 Similarly, for the entire year of 2019, NSPIKES (335 Å) yields an $r = 0.39$ and a $\rho =$
 265 0.37 when compared against Kp, an $r = 0.37$ and a $\rho = 0.39$ when compared against
 266 ap and an $r = -0.42$ and a $\rho = -0.38$ when compared against Sym-H.

267 The time lag between the geomagnetic parameters drop or increase with the cor-
 268 responding increase of NSPIKES observed during the month of February 2019 is stud-
 269 ied in the bottom right plot of Figure 6. More specifically, seven positive and seven neg-
 270 ative 3 hour (time cadence) shifts are performed on the NSPIKES data and the differ-
 271 ent Pearson correlation coefficients are calculated for each shift. A positive lag (shift)
 272 means that Kp leads NSPIKES by $\Delta t \in [3, 6, 9, 12, 15]$ h while a negative lag means that
 273 NSPIKES leads Kp by the same Δt time intervals. The highest correlation value is recorded
 274 for a positive 3 hour shift and it can be assumed to be of no significance -especially for
 275 Kp and ap- as the parameters are a 3 hour standardized mean.

Wavelength (Å)	94	131	171	193	211	304	335
Pearson Correlation (r)							
Kp	0.262 ± 0.12	0.285 ± 0.09	0.346 ± 0.03	0.312 ± 0.11	0.307 ± 0.11	0.341 ± 0.05	0.284 ± 0.13
ap	0.227 ± 0.12	0.248 ± 0.09	0.305 ± 0.06	0.273 ± 0.10	0.265 ± 0.11	0.297 ± 0.06	0.243 ± 0.13
SymH	0.265 ± 0.12	0.285 ± 0.09	0.326 ± 0.05	0.292 ± 0.10	0.293 ± 0.11	0.321 ± 0.05	0.266 ± 0.13
Spearman Correlation (ρ)							
Kp	0.264 ± 0.04	0.258 ± 0.04	0.309 ± 0.04	0.312 ± 0.04	0.306 ± 0.04	0.315 ± 0.04	0.314 ± 0.04
ap	0.274 ± 0.04	0.268 ± 0.04	0.323 ± 0.04	0.326 ± 0.04	0.319 ± 0.04	0.328 ± 0.04	0.327 ± 0.04
SymH	0.296 ± 0.04	0.292 ± 0.04	0.322 ± 0.03	0.324 ± 0.03	0.323 ± 0.03	0.329 ± 0.03	0.328 ± 0.03

Table 1: Ten year (2011-2021) mean Pearson and Spearman correlation coefficients for NSPIKES when compared with the three geomagnetic parameters (Kp, ap and Sym-H) for the seven different AIA wavelengths. In blue are marked the highest correlation values for each one of the geomagnetic indices.

276 The Pearson and Spearman correlation coefficients for the seven different NSPIKES
 277 wavelengths ($\lambda \in [94, 131, 171, 193, 211, 304, 335] \text{ \AA}$) when compared to the three dif-
 278 ferent correlation coefficients (Kp, ap and Sym-H) are presented in Table 1. The results
 279 presented are the mean of the yearly correlations for a ten year period (2011-2021). The
 280 highest values (marked in blue) for ap and Sym-H are the Spearman’s correlations ob-
 281 served for $\lambda = 304 \text{ \AA}$. For Kp the Pearson linear correlation scores for $\lambda = 171 \text{ \AA}$ is
 282 the highest value. Note that for the Sym-H parameter only the absolute values of r and
 283 ρ are recorded as its correlation to NSPIKES is negative. In the next chapters a simi-
 284 lar analysis will be performed when the NSPIKES are compared to the readings of the
 285 GOES-14 electron and proton detection instruments.

286 **5 Correlation with GOES-14 Data**

287 As mentioned in Section 2, SDO is in a circular geosynchronous orbit at an alti-
 288 tude of 35,789 km (22,238 mi), at 102° West longitude, inclined at 28.5° . This means that
 289 twice a day SDO passes through the equator where it comes in very close proximity (\approx
 290 1,642 km) to the GOES-14 satellite which is in a geostationary orbit at 105° West lon-
 291 gitude at an altitude of 35,773 km (22,228 mi). This means that twice a day we get a
 292 chance to compare the SDO spike data with the GOES-14 proton and electron readings.

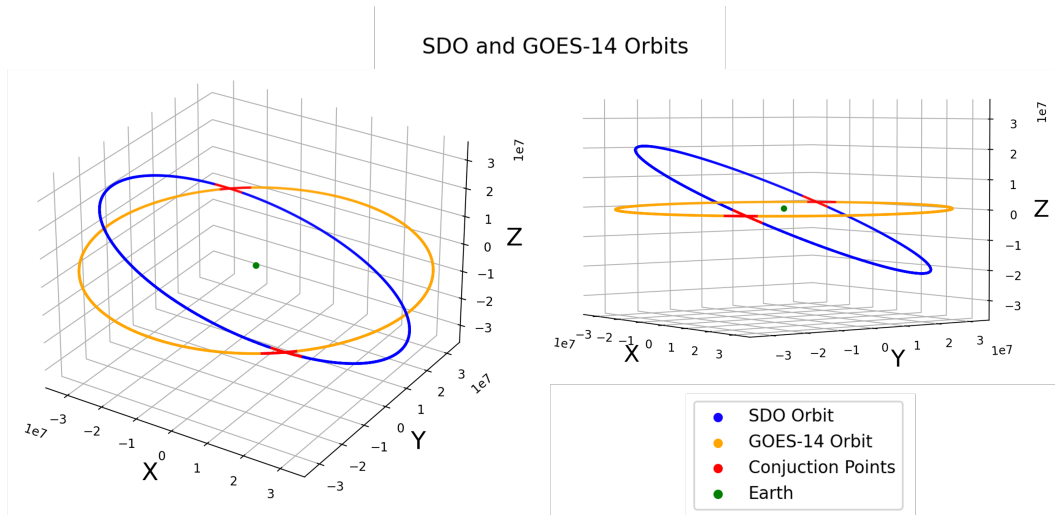


Figure 7: Three-dimensional plot of the SDO (blue) and GOES-14 (orange) orbits in the GEI coordinate system. In red are the conjunction parts of the orbits ($z_{SDO} = \pm 2,000 \text{ km}$) and in green is the center of the coordinate system, the Earth.

293 Figure 7 shows the orbits of the SDO (blue) and GOES-14 (orange) satellites in
 294 the Geocentric Equatorial Inertial System (GEI), while in red is the part of the orbits
 295 where the two satellites “meet”. In the rest of the paper we will be denoting as “Equa-
 296 tor Data” the SDO and GOES-14 readings obtained at the part of the orbits highlighted
 297 in red. The GEI system has its x -axis pointing from the Earth towards the first point
 298 of Aries (the position of the Sun at the vernal equinox). This direction is the intersec-
 299 tion of the Earth’s equatorial plane and the ecliptic plane and thus the x -axis lies in both
 300 planes. The z -axis is parallel to the rotation axis of the Earth and y completes the right-
 301 handed orthogonal set.

302 GOES-14 (known as GOES-O prior to reaching its operational orbit) is a weather
 303 satellite, which was built by Boeing and is part of the US National Oceanic and Atmo-

304 spheric Administration’s (NOAA) Geostationary Operational Environmental Satellite
 305 (GOES) system. It is equipped with nine different instruments⁷ including the EPS/HEPAD
 306 (Energetic Particle Sensors / High Energy Proton and Alpha Detector, Hanser (2011))
 307 which is part of the overall SEM (Space Environment Monitor) and whose data is used
 308 in this research. The EPS consists of two energetic proton, electron and alpha detectors
 309 (EPEAD), a magnetospheric proton detector (MAGPD) and a magnetospheric electron
 310 detector (MAGED). The data from all three detectors are used in this research to cal-
 311 culate their readings’ correlations with the SDO NSPIKES values and explore the nature
 312 of the AIA spikes.

313 This equator region where the orbits intersect is at the geographic equator. This
 314 is generally close to the latitude of minimum magnetic field strength for each field line.
 315 Under the dipole model and non-dipolar typical geomagnetic conditions, this is at the
 316 magnetic equator. This latitude of minimum magnetic field strength has the property
 317 that mirroring radiation belt particles of all pitch angles will pass through it at some point
 318 during their bounce motion. While not exactly at the latitude of minimum magnetic field
 319 strength, we are close to it. This gains us the insight that the satellite is exposed to nearly
 320 all bouncing particles from this location, with detections limited only by the field-of-view
 321 of the virtual detector.

322 5.1 NSPIKES Correlation with Electrons

323 The Magnetospheric Electron Detector (MAGED) is a set of nine collimated solid
 324 state telescopes (Rowland & Weigel, 2012) each with a 30° full-angle conical field of view,
 325 that form a cruciform field of regard with the central telescope pointing anti-earthward.
 326 The telescopes collect magnetospheric electrons and provide electron flux measurements
 327 in five energy channels that range from 30 keV to 600 keV (30–50, 50–100, 100–200, 200–350,
 328 and 350–600 keV). For each channel the number of electrons is counted in units of $e^-/(cm^2$
 329 $sr keV s)$. The MAGED archival flux data are provided as directional differential elec-
 330 tron fluxes determined for the midpoint of the five energy ranges (i.e., at 40, 75, 150, 275,
 331 and 475 keV, (Sillanpää et al., 2017)).

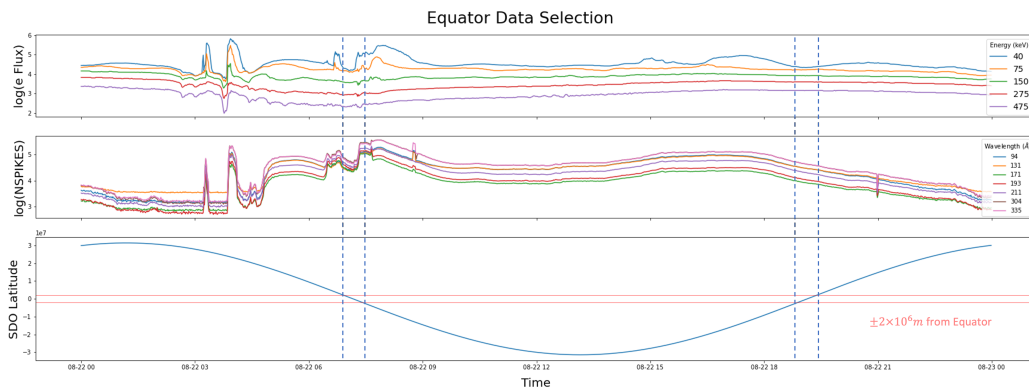


Figure 8: Plots of the GOES-14 MAGED Electron Flux (Telescope 2) and the SDO NSPIKES in logarithmic scale and the SDO Latitude against time for a single day (August 22, 2018). The horizontal dotted lines define the latitude interval in which Electron Flux and NSPIKES values will be considered as “Equator Data”.

⁷ https://space.oscar.wmo.int/satellites/view/goes_14

332

333

334

335

336

337

338

339

340

341

342

343

Figure 8 shows how the SDO NSPIKES and GOES-14 Electron Flux values in logarithmic scale vary against time for a single day (August 22, 2018), along with the corresponding SDO Latitude (z-axis) values at each moment (1m cadence). As equator data (red in Figure 7) we chose the data at the times where SDO passes through the equator, i.e. the times where SDO is within 2000 km from the equator ($z_{SDO} = \pm 2000$ km). Therefore, the correlation analysis presented below will be done for three different domains: first we analyze the entirety of the NSPIKES and Electron Flux data (Full Orbit), we then concentrate only on assessing the correlation of the data intervals that lie between the dotted lines of Figure 8 (Equator) and lastly for comparison reasons we also compute the correlation for the times where SDO is not in close proximity to GOES-14 (Non-Equator).

MAGED Electron Flux	40 keV	75 keV	150 keV	275 keV	475 keV
Pearson Correlation (r)					
Equator	0.629 ± 0.262	0.571 ± 0.239	0.404 ± 0.174	0.319 ± 0.158	0.280 ± 0.151
Non-Equator	0.513 ± 0.209	0.516 ± 0.210	0.434 ± 0.179	0.347 ± 0.150	0.290 ± 0.131
Full Orbit	0.515 ± 0.210	0.515 ± 0.210	0.430 ± 0.178	0.345 ± 0.150	0.289 ± 0.132
Spearman Correlation (ρ)					
Equator	0.729 ± 0.009	0.712 ± 0.011	0.670 ± 0.025	0.611 ± 0.036	0.550 ± 0.039
Non-Equator	0.529 ± 0.017	0.526 ± 0.007	0.499 ± 0.004	0.456 ± 0.010	0.412 ± 0.013
Full Orbit	0.534 ± 0.016	0.530 ± 0.006	0.504 ± 0.004	0.460 ± 0.011	0.416 ± 0.014

Table 2: Pearson and Spearman correlation values for NSPIKES and MAGED Electron Flux data for the five different MAGED energy channels, calculated over a period of 27 months (December 2017 to February 2020). The nine different MAGED telescopes and seven different AIA wavelengths are accounted for by presenting the mean and standard deviation of all possible combinations. In blue, are marked the highest correlation values for each different SDO and GOES satellite location.

344

345

346

347

348

349

350

351

To determine the origins of the spikes in the AIA images, we first study the association of the NSPIKES parameter with the MAGED Electron Flux data. Table 2 presents the Pearson and Spearman correlation values between NSPIKES and MAGED Electron Fluxes for the entire uninterrupted period when SDO and GOES-14 were both operational (December 2017 to February 2020). For each one of the five different MAGED channels, the mean value and standard deviation for all different combinations of MAGED telescopes and AIA wavelengths is recorded. Separate correlations are also calculated for the Equator and Non-Equator periods as seen and described in Figure 7.

352

353

354

355

356

357

358

359

360

361

362

For all the cases studied, the Spearman correlation values are higher ($\rho - r = 0.116 \pm 0.091$) than the respective Pearson ones suggesting that the relationship between NSPIKES and MAGED Electron Fluxes is not exactly linear but it can better be described by a monotonically increasing function. Low energy electrons (ex. 40 and 75 keV channels) show always higher association with NSPIKES. Hence, the low energy MAGED electron channel of 40 keV is the one that can be better associated with NSPIKES having a Spearman correlation of $\rho = 0.729 \pm 0.009$ at the equator. Lastly, as expected due to the SDO and GOES-14 satellites being in close proximity and therefore study the same space within the radiation belt, the Equator correlation values are most of the times higher than the Non-Equator ones by $\Delta\rho = 0.170$ and $\Delta r = 0.021$ ($\rho_{eq} - \rho_{non} = 0.170 \pm 0.022$ and $r_{eq} - r_{non} = 0.021 \pm 0.057$). It is noteworthy that for satellite data which

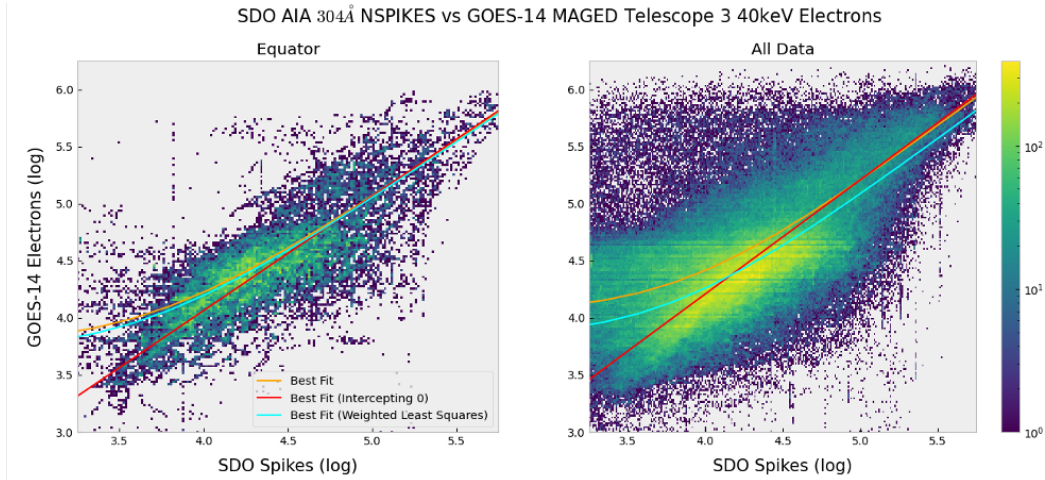


Figure 9: Heatmaps for the Equator and Full Orbit NSPIKES and MAGED Electrons data in logarithmic scale. The correlation values for the Equator data are $r = 0.779$ and $\rho = 0.753$.

363 are prone to a significant amount of noise, a Pearson and Spearman value greater than
 364 0.5 can be considered as a relatively strong correlation.

365 Although Table 2 presents the mean values across different MAGED telescopes and
 366 AIA wavelengths, there are specific cases where the association between NSPIKES and
 367 MAGED electrons can be even higher. One of these cases is when we compare the num-
 368 ber of spikes detected in the $\lambda = 304 \text{ \AA}$ AIA images to the 40 keV electrons detected
 369 by the third MAGED detector (Telescope 3) from December 2017 to February 2020. Fig-
 370 ure 9 includes the two dimensional histograms (heatmaps) for these specific NSPIKES
 371 and MAGED electron values, both for the full orbits (a) and the equator intervals (b).
 372 The fact that the AIA 304Å images are the least bright compared to other wavelengths,
 373 might be a possible explanation for why this wavelength channel yields better correla-
 374 tion values, as it can capture more accurately particles of non-solar origin.

375 On the left heatmap of Figure 9 the Equator AIA 304 Å NSPIKES are put in 300
 376 bins and are plotted against the respective MAGED Telescope 3 40 keV Electrons (also
 377 split in 300 bins) in logarithmic scale for the time period between December 2017 to Febru-
 378 ary 2020. The right heatmap presents the same data but for the full satellite orbits. The
 379 Pearson and Spearman values for the Equator data are $r = 0.779$ and $\rho = 0.753$ re-
 380 spectively. All plots include the best fit lines in orange, the best fit lines forced to inter-
 381 cept $(0, 0)$ in red and the weighted ($w = 1/x$) least squares lines in cyan. The trend
 382 where Equator data associate better with each other holds true for this case too.

383 The issue of the bias in the correlation is dealt with carefully. It is possible that
 384 spikes originate from multiple, independent processes. In addition to the source of ra-
 385 diation belt particle impacts, other sources could include (a) arcing due to differential
 386 charging or (b) galactic cosmic rays impacts. Processes such as (a) or (b) will necessar-
 387 ily generate spikes at a constant background level when averaged over these several years.
 388 This is due to their independence from the radiation belt enhancements: radiation belt
 389 enhancements do not contribute to differential charging, and the galactic cosmic ray ar-
 390 rival rate does not depend strongly on either radiation belt enhancements or magneto-
 391 spheric reconfigurations. Therefore, they collectively would appear in Figure 9 as a con-
 392 stant bias term. Because we do not know for sure whether these additional possible sources
 393 arise in reality, we model with and without a bias term.

394 The second electron-detecting instrument onboard of GOES-14 is the Energetic Pro-
 395 ton Electron and Alpha Detector (EPEAD), which observes electrons in the energy range
 396 above that of MAGED. There are two EPEADs on GOES-14, one with a field-of-view
 397 (spacecraft $+x$ direction) to the east, and the other with field-of-view to the west (space-
 398 craft $-x$ direction). The results that the two EPEADS yield when compared to the NSPIKES
 399 are almost identical therefore for simplicity in this report we only present the EPEAD
 400 East results. More specifically, EPEAD East gives us the dead-time corrected average
 401 flux of electrons from the E1 channel with effective energy > 0.8 MeV with backgrounds
 402 and proton contamination removed (if contamination is too severe, fluxes are replaced
 403 with fill values, but this is rare in the E1 channel). EPEAD also measures > 2 MeV and
 404 > 4 MeV electron fluxes. However, because these channels exhibit extended periods when
 405 the electron fluxes are below backgrounds, they were not used in the correlation anal-
 406 ysis.

EPEAD	Spearman Correlation (ρ)						
Wavelength (\AA)	94	131	171	193	211	304	335
Equator	0.529	0.534	0.432	0.435	0.456	0.448	0.447
Non-Equator	0.383	0.385	0.350	0.350	0.357	0.350	0.350
Full Orbit	0.387	0.389	0.351	0.352	0.359	0.352	0.352

Table 3: Spearman correlation values for NSPIKES and EPEAD > 0.8 MeV (E1) electron flux data for the seven different AIA wavelengths, calculated over a period of 27 months (December 2017 to February 2020).

407 The relationship between SDO NSPIKES and EPEAD Electrons is highly non-linear
 408 therefore Table 3 presents only the Spearman Correlation values for different AIA wave-
 409 lengths. Similarly to the MAGED data, the EPEAD Electron data correlates better with
 410 SDO's NSPIKES at the equator compared to the rest of the orbit, showing an increase
 411 in Spearman correlation of $\Delta\rho = \rho_{eq} - \rho_{non} = 0.108 \pm 0.026$. Out of the seven AIA
 412 wavelengths, the best association between the two data products is for $\lambda = 131 \text{ \AA}$ where
 413 $\rho = 0.534$ at the SDO and GOES-14 orbits conjunction points.

414 In conclusion, this section shows that the SDO AIA NSPIKES header variable as-
 415 sociates very well with the electron readings from two different GOES-14 detectors, the
 416 MAGED and the EPEAD, especially when the two satellites are in close proximity twice
 417 a day. The evidence presented suggest that the spikes detected in the SDO's AIA im-
 418 ages are caused mostly by energetic electrons that reside within the radiation belt, rather
 419 than protons. To strengthen this argument, in Section 5.2 we follow a similar NSPIKES
 420 correlation approach for protons.

421 5.2 NSPIKES Correlation with Protons

422 The third GOES-14 detector whose data we compare to the SDO AIA spikes is the
 423 Magnetospheric Proton Detector (MAGPD). Similar to MAGED, MAGPD has nine tele-
 424 scopes with fields-of-view at the $-Z$ direction, pointing away from the earth. The instru-
 425 ment collects magnetospheric protons and provides proton flux measurements ranging
 426 from 80 keV to 800 keV in five separate channels which have mean flux detection val-
 427 ues of 95, 140, 210, 300 and 575 keV and are corrected for dead time.

428 Similarly to the MAGED and EPEAD instruments, for all the different cases stud-
 429 ied in Table 4, the Spearman correlation values are higher ($\rho-r = 0.180 \pm 0.040$) than
 430 the respective Pearson ones, suggesting that the relationship between NSPIKES and MAGPD
 431 Proton Fluxes is not linear either and it can be better described by a monotone func-

MAGPD Proton Flux	95 keV	140 keV	210 keV	300 keV	575 keV
Pearson Correlation (r)					
Equator	0.132 ± 0.083	0.156 ± 0.091	0.190 ± 0.101	0.211 ± 0.117	0.192 ± 0.106
Non-Equator	0.149 ± 0.069	0.173 ± 0.080	0.201 ± 0.096	0.234 ± 0.107	0.212 ± 0.098
Full Orbit	0.148 ± 0.070	0.172 ± 0.081	0.209 ± 0.096	0.233 ± 0.108	0.211 ± 0.098
Spearman Correlation (ρ)					
Equator	0.326 ± 0.052	0.357 ± 0.052	0.423 ± 0.050	0.467 ± 0.0476	0.447 ± 0.042
Non-Equator	0.306 ± 0.019	0.329 ± 0.018	0.370 ± 0.017	0.389 ± 0.016	0.345 ± 0.014
Full Orbit	0.305 ± 0.020	0.328 ± 0.019	0.370 ± 0.018	0.390 ± 0.017	0.347 ± 0.015

Table 4: Pearson and Spearman correlation values for NSPIKES and MAGPD Proton Flux data for the five different MAGPD energy channels, calculated over a period of 27 months (December 2017 to February 2020). The nine different MAGPD telescopes and seven different AIA wavelengths are accounted for by presenting the mean and standard deviation of all possible combinations. In blue are marked the highest correlation values for each different SDO and GOES satellite location.

432 tion. Note that the MAGPD $\rho-r$ is higher compared to MAGED, with proton Pear-
 433 son results being in the majority of the studies < 0.2 suggesting that there is no signif-
 434 icant linear correlation. High energy protons (ex. 300 and 575 keV channels) show al-
 435 ways higher association with NSPIKES. Hence, the second highest energy MAGPD pro-
 436 ton channel of 300 keV is the one that can be better associated with NSPIKES having
 437 a Spearman correlation of $\rho = 0.467 \pm 0.0476$ at the equator. Lastly, as observed in
 438 all the studies in Section 5.1, the Spearman correlation Equator values are always higher
 439 than the Non-Equator ones by $\Delta\rho = \rho_{eq} - \rho_{non} = 0.056 \pm 0.030$.

440 Although the Spearman correlation values for the MAGPD protons are in the ma-
 441 jority of the case studies inferior to the ones calculated for the MAGED and EPEAD pro-
 442 tons, a Pearson value of $\rho \in [0.3, 0.5]$ suggests that there is some correlation. To inves-
 443 tigate whether protons in the MeV energy range, that is typically associated with spikes
 444 in solar images (e.g., SOHO EIT), contribute to AIA spike data, we study the fluctu-
 445 ation of the NSPIKES variable during large Solar Energetic Particle (SEP) events of So-
 446 lar Cycle 24.

447 Figure 10 shows the evolution of the NSPIKES (304 Å) variable during the three
 448 most significant (highest proton flux at $> 10 \text{ MeV}^8$) SEP events that NOAA observed
 449 (Rodríguez et al., 2014) since the beginning of the SDO mission (July 2010). Such events
 450 have been thoroughly studied (Cliver, 2008; Reames, 2013) and used before in space weather
 451 prediction applications (Whitman et al., 2022; Kasapis et al., 2022). Research has shown
 452 (Lanzerotti, 1968; G. A. Paulikas & Blake, 1969; Fillius, 1968) that during such events,
 453 the proton content in the earth magnetosphere increases drastically which would mean
 454 that spikes due to protons in SDO’s AIA images would increase too (Lario, 2005; Matthiä
 455 et al., 2009; Kress et al., 2013; Rodríguez et al., 2010). As it can be observed in Figure
 456 10, the NSPIKES data does not show any significant increase during the beginning (green
 457 dotted lines) nor during the maximum (red dotted lines) of these three significant SEP
 458 events as it has been recorded by GOES-13 based on proton flux (yellow). We note that
 459 there is a brief period around 2012-Jan-24T15:30 during which a strong magnetospheric
 460 compression occurred. The 30-600 keV radiation belt electron flux (not shown) increased
 461 due to the compression, while the increase in the ongoing solar particle event fluxes was

⁸ <https://umbra.nascom.nasa.gov/SEP/>

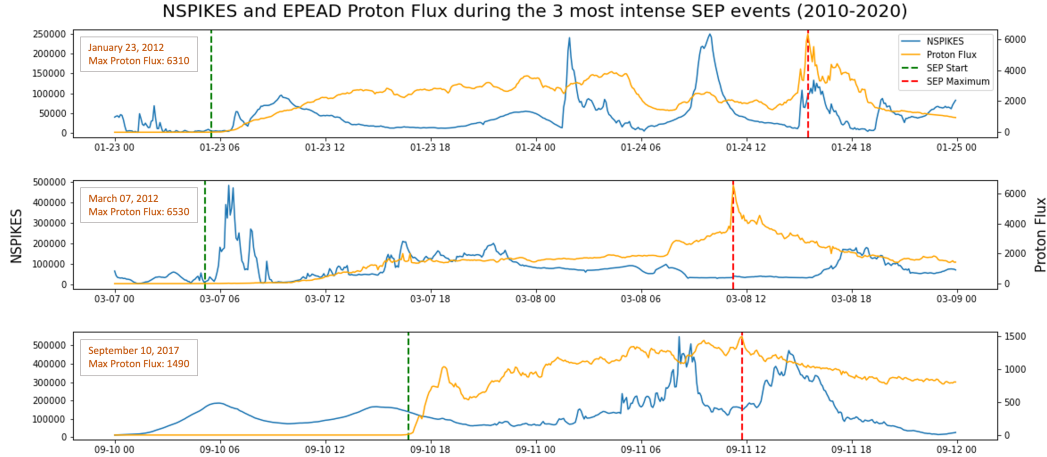


Figure 10: NSPIKES at 304 Å (blue) and EPEAD > 10 MeV proton (yellow) time profiles for the two-day periods that include the three most significant SEP events recorded by NOAA during the first decade of operation of the SDO. The green dotted lines signify the beginning of the SEP events and the red dotted line signifies the time of maximum flux of the events as defined by NOAA.

462 due to acceleration by the shock prior to arrival at Earth. SDO was at the highest lat-
 463 titude in its orbit. This analysis indicates that spike correlation with proton flux may be
 464 an inherited (non-causal) correlation due to the fact that regions of high electron fluxes
 465 in the magnetosphere can also have high proton fluxes.

466 6 Discussion

467 The association of the SDO spike data with the GOES-14 electrons and proton fluxes
 468 is especially useful for characterizing the radiation belt at non-equatorial latitudes where
 469 measurements are not available. Solar research, which uses data from satellites such as
 470 SOHO, has measured direct proton hits on CCD cameras (Didkovsky et al., 2006) within
 471 and outside the solar disk. Unlike SOHO, which orbits around the first Lagrangian point
 472 (L1), SDO's geosynchronous orbit intersects the outer radiation belt, indicating electron
 473 hits should be considered too.

474 It can be observed throughout the paper that the NSPIKES correlation tests are
 475 more sensitive to low electron energies. As it can be seen in Table 2 and Table 3, MAGED
 476 low energy electrons (ex. 40 and 75 keV channels) show always higher association with
 477 NSPIKES -regardless of the AIA EUV channel- compared to MAGED higher-energy chan-
 478 nels and EPEAD. This might be counterintuitive as higher energy electrons should be
 479 able to penetrate the AIA telescope's protective shield easier than lower energy electrons,
 480 but our research efforts suggest that this might be a partly statistical outcome due to
 481 having many more particle hits from lower energy MAGED channels (Figure 8). The op-
 482 posite trend can be observed for the MAGPD protons, where higher energy channels cor-
 483 relate better with NSPIKES. However, this increase may be correlative and not causative,
 484 as proton flux is correlated with electron flux.

485 While desirable to have, it is likely challenging to calculate a per-energy response
 486 function for the virtual electron detector from on-orbit data. However, an attempt could
 487 be made (and is left for future work), where in the response function is modeled as a lin-

ear regression. To do this, one would model the NSPIKES variable as a linear combination of the fluxes at available energies. By solving for the weights in this (very) over-determined system, the response at each energy could be found. Because the fluxes are correlated with each other, this regression should be done carefully and the co-variance matrix should be analyzed. Limitations to this approach are that the response function may depend on fluxes at energies not measured by GOES instrumentation.

$$NSPIKES = \sum_{k=0}^{N_E} w_k \text{Flux}(E_k) + \text{Bias} \quad (1)$$

Another desirable parameter left for future analysis is that of the field of view associated with this virtual detector. This field of view would give insight into the pitch angle coverage, through coupling with a magnetic field model to provide the magnetic field direction. Because SDO is always pointed towards the sun, the pitch angle span could be calculated geometrically from the aperture size, the CCD size, and the distance from the aperture to the CCD. We note that as SDO goes to higher magnetic latitudes, the extent will stay the same, but the center of the extent will sample a very different portion of pitch angles. Future analysis may show that this provides a natural "scanning" mechanism to gain coverage of much of pitch angle space.

There are studies of images that are primarily influenced by proton flux. Our results do not indicate that it is impossible for protons to also contribute to the AIA spike population. Instead, they simply indicate that the electrons have a much stronger influence because of the high energetic electron population in the Earth's magnetosphere. Studies such as Didkovsky et al. (2006) were performed using instruments in the solar wind, with different plasma environments. The focus of the paper is on determining the radiation belt measurements that correlate most highly with AIA spikes in order to use AIA as a proxy measurement. The influence of SEPs and cosmic rays is not significant at the GOES-14 Geostationary Equatorial Orbit relative to the high flux of radiation belt electrons.

In this paper, we prove that NSPIKES are a proxy for electrons (especially around the 40 keV range), therefore in future work NSPIKES can be used to a) determine the L dependence of those electrons, b) specify model plasma boundary conditions outside the geosynchronous orbit and c) see particle injections before they hit GEO. Although a strong linear correlation was found, there is some dispersion in the values. There are a number of potential factors that could contribute. First, SDO and GOES-14 are not at the exact same location, even when both were near the equator, so some difference in values can be expected. Second, SDO/AIA and GOES-14 have different detectors, and AIA was not designed as a particle detector. In Figure 4 the location of the detected spikes indicates that the spike detection algorithm is more efficient in dark regions of the image; therefore there will be some fluctuation in detection efficiency. Finally, there is some correlation with higher electron energies and proton flux too; this study only examines correlation and not direct cause of particle hits. It is likely that different populations have contributions to the number of spikes, but the 40 keV electron flux is highest and therefore has the greatest correlation. Future studies can examine factors such as spacecraft geometry, and orientation relative to the direction of the magnetic field lines, and explicit comparison of the magnetosphere at different levels of radiation belt activity may shed more light on this. If successful, this could allow proxy measurements of electron flux at higher latitudes instead of just equatorial latitudes.

7 Conclusion

SDO is a solar mission that goes out of the ecliptic and can be used to measure electron densities on a unique orbit. Because SDO is in an inclined geosynchronous orbit, the spacecraft passes through regions of high plasma density in the outer radiation belt. Although SDO’s Atmospheric Imaging Assembly consists of solar telescopes deployed to image the Sun, AIA’s CCD detector is also sensitive to direct hits from magnetospheric electrons. These impacts show up as small ”spikes” in the images. As a part of data processing to create science-quality images, an algorithm removes the spikes from each of the images. The number of spiked pixels removed from the image is reported in the meta-data, as a value labeled NSPIKES.

In this work we examine for the first time the behavior of NSPIKES, which is usually treated as a data artifact. We compared with global geomagnetic parameters K_p , a_p , and Sym-H as a simple test to illustrate that the NSPIKES value does fluctuate with geomagnetic activity. However, the correlation was not strong; this is not surprising because the processes causing geomagnetic fluctuations and those that determine particle populations are related but not perfectly correlated.

We then examine the correlation of SDO spikes to directly measured proton and electron fluxes from the GOES-14 spacecraft which twice a day comes close to SDO (within 1700 km). We find that AIA spikes are highly correlated with the GOES-14 electrons detected by the MAGED and EPEAD instruments at the equator (where the two satellites meet) with Spearman’s Correlation values of $\rho = 0.73$ and $\rho = 0.53$ respectively, while a weaker correlation of $\rho = 0.47$ is shown with MAGPD protons. In particular, it was found that the correlation was highest ($r = 0.78$) for GOES-14 MAGED 40 keV electrons, and had a linear relationship:

$$J_{GOESe,40keV} = 1.1604 \text{ NSPIKES} \quad (2)$$

This indicates that a) the SDO NSPIKES value can be used as a very good proxy measurement for 40 keV electron flux after the end of GOES-14 measurements in 2019, and b) SDO has the potential to produce electron proxy measurements far out of the ecliptic as well. In fact, sudden dropouts in the number of spikes were observed, coinciding with higher latitude passes in SDO’s 28.5° inclined orbit; these periods seem to be consistent with possible locations of the polar cusp. Further examination of these flux dropout locations with geomagnetic models are planned as future work.

In conclusion, in this work we show that the SDO/AIA spiked pixels can help characterize the radiation belt in areas where other measurements aren’t available, therefore creating a new dataset with proxy measurements from electrons of the outer radiation belt, within and out of the equator, turning the radiation belt characterization into a three-dimensional structure.

Acknowledgments

We thank Mark Moldwin from the University of Michigan, Climate and Space Sciences and Engineering Department and the NASA Michigan Space Grant Consortium who partially funded Spiridon Kasapis’ summer internship at NASA Goddard Space Flight Center. All SDO data used in this study are available from the Joint Science Operations Center (JSOC) NASA grant (see <http://jsoc.stanford.edu/>). The GOES-14 data used in this study are available from the NOAA National Centers for Environmental Information (<https://ngdc.noaa.gov/stp/satellite/goes/dataaccess.html>). Juan Rodriguez was supported by NOAA cooperative agreement NA17OAR4320101. Barbara Thompson was supported by the NASA Internal Funding Science Model (ISFM) Center for HelioAnalytics Project. The files that include the algorithms used in this study

579 can be found here: https://github.com/skasapis/sdo_rad_belt. T. Paul O'Brien is
580 acknowledged for his significant contribution and insightful comments on this work.

581

References

- 582 Cai, L., Ma, S., Cai, H., Zhou, Y., & Liu, R. (2009). Prediction of sym-h index
583 by narx neural network from imf and solar wind data. *Science in China Series E:
584 Technological Sciences*, 52(10), 2877–2885.
- 585 Carlton, A., Pich, M. d. S.-S., Kim, W., Jun, I., & Cahoy, K. (2018). Using the
586 galileo solid-state imaging instrument as a sensor of jovian energetic electrons.
587 *IEEE Transactions on Nuclear Science*, 66(1), 255–261.
- 588 Cliver, E. W. (2008). History of research on solar energetic particle (sep) events: the
589 evolving paradigm. *Proceedings of the International Astronomical Union*, 4(S257),
590 401–412.
- 591 Didkovsky, L., Judge, D., Jones, A., Rhodes Jr, E., & Gurman, J. (2006). Measuring
592 proton energies and fluxes using eit (soho) ccd areas outside the solar disk images.
593 *Astronomische Nachrichten: Astronomical Notes*, 327(4), 314–320.
- 594 Fillius, R. W. (1968). Penetration of solar protons to four earth radii in the equato-
595 rial plane. In *Iaga comm. 5, solar-terrest. and cosmic-terrest. relationship conf.*
- 596 Hanser, F. (2011). Eps/hepad calibration and data handbook. *Assurance Technology
597 Corporation, Carlisle, Mass.*
- 598 Kasapis, S., Zhao, L., Chen, Y., Wang, X., Bobra, M., & Gombosi, T. (2022). Inter-
599 pretable machine learning to forecast sep events for solar cycle 23. *Space Weather*,
600 20(2), e2021SW002842.
- 601 Kirk, M. S., Balasubramaniam, K., Jackiewicz, J., & Gilbert, H. R. (2017). The ori-
602 gin of sequential chromospheric brightenings. *Solar Physics*, 292(6), 1–21.
- 603 Kirk, M. S., Balasubramaniam, K., Jackiewicz, J., & McAteer, R. J. (2014). Qual-
604 ities of sequential chromospheric brightenings observed in $h\alpha$ and uv images. *The
605 Astrophysical Journal*, 796(2), 78.
- 606 Kress, B., Rodriguez, J., Mazur, J., & Engel, M. (2013). Modeling solar proton ac-
607 cess to geostationary spacecraft with geomagnetic cutoffs. *Advances in Space Re-
608 search*, 52(11), 1939–1948.
- 609 Kurth, W., De Pascuale, S., Faden, J., Kletzing, C., Hospodarsky, G., Thaller, S., &
610 Wygant, J. (2015). Electron densities inferred from plasma wave spectra obtained
611 by the waves instrument on van allen probes. *Journal of Geophysical Research:
612 Space Physics*, 120(2), 904–914.
- 613 Lanzerotti, L. (1968). Penetration of solar protons and alphas to the geomagnetic
614 equator. *Physical Review Letters*, 21(13), 929.
- 615 Lanzerotti, L., Roberts, C., & Brown, W. (1967). Temporal variations in the elec-
616 tron flux at synchronous altitudes. *Journal of Geophysical Research*, 72(23), 5893–
617 5902.
- 618 Lario, D. (2005). Advances in modeling gradual solar energetic particle events. *Ad-
619 vances in Space Research*, 36(12), 2279–2288.
- 620 Lemen, J. R., Akin, D. J., Boerner, P. F., Chou, C., Drake, J. F., Duncan, D. W.,
621 ... others (2011). The atmospheric imaging assembly (aia) on the solar dynamics
622 observatory (sdo). In *The solar dynamics observatory* (pp. 17–40). Springer.
- 623 Lezniak, T., Arnoldy, R., Parks, G., & Winckler, J. (1968). Measurement and inten-
624 sity of energetic electrons at the equator at 6.6 r e. *Radio Science*, 3(7), 710–714.
- 625 Li, W., & Hudson, M. (2019). Earth’s van allen radiation belts: From discovery
626 to the van allen probes era. *Journal of Geophysical Research: Space Physics*,
627 124(11), 8319–8351.
- 628 Li, X., Baker, D., Kanekal, S., Looper, M., & Temerin, M. (2001). Long term mea-
629 surements of radiation belts by sampex and their variations. *Geophysical Research
630 Letters*, 28(20), 3827–3830.
- 631 Matthiä, D., Heber, B., Reitz, G., Meier, M., Sihver, L., Berger, T., & Herbst, K.
632 (2009). Temporal and spatial evolution of the solar energetic particle event on
633 20 january 2005 and resulting radiation doses in aviation. *Journal of Geophysical*

- 634 *Research: Space Physics*, 114(A8).
- 635 Matzka, J., Stolle, C., Yamazaki, Y., Bronkalla, O., & Morschhauser, A. (2021). The
636 geomagnetic kp index and derived indices of geomagnetic activity. *Space Weather*,
637 19(5), e2020SW002641.
- 638 Menvielle, M., & Berthelier, A. (1991). The k-derived planetary indices: Description
639 and availability. *Reviews of Geophysics*, 29(3), 415–432.
- 640 Paulikas, G., & Blake, J. (1979). Effects of the solar wind on magnetospheric dy-
641 namics: Energetic electrons at the synchronous orbit. *Quantitative Modeling of*
642 *Magnetospheric Processes, Geophys. Monogr. Ser.*, 21, 180–202.
- 643 Paulikas, G. A., & Blake, J. B. (1969). Penetration of solar protons to synchronous
644 altitude. *Journal of Geophysical Research*, 74(9), 2161–2168.
- 645 Pearson, K. (1896). Vii. mathematical contributions to the theory of evolution.—iii.
646 regression, heredity, and panmixia. *Philosophical Transactions of the Royal Society*
647 *of London. Series A, containing papers of a mathematical or physical charac-*
648 *ter*(187), 253–318.
- 649 Pesnell, W. D., Thompson, B. J., & Chamberlin, P. (2011). The solar dynamics ob-
650 servatory (sdo). In *The solar dynamics observatory* (pp. 3–15). Springer.
- 651 Rangarajan, G., & Lyemori, T. (1997). Time variations of geomagnetic activity in-
652 dices kp and ap: an update. In *Annales geophysicae* (Vol. 15, pp. 1271–1290).
- 653 Reames, D. V. (2013). The two sources of solar energetic particles. *Space Science*
654 *Reviews*, 175(1), 53–92.
- 655 Rodriguez, J., Krossschell, J., & Green, J. (2014). Intercalibration of goes 8–15 solar
656 proton detectors. *Space Weather*, 12(1), 92–109.
- 657 Rodriguez, J., Onsager, T., & Mazur, J. (2010). The east-west effect in solar proton
658 flux measurements in geostationary orbit: A new goes capability. *Geophysical Re-*
659 *search Letters*, 37(7).
- 660 Rowland, W., & Weigel, R. S. (2012). Intracalibration of particle detectors on a
661 three-axis stabilized geostationary platform. *Space Weather*, 10(11).
- 662 Scherrer, P. H., Schou, J., Bush, R., Kosovichev, A., Bogart, R., Hoeksema, J., ...
663 others (2012). The helioseismic and magnetic imager (hmi) investigation for the
664 solar dynamics observatory (sdo). *Solar Physics*, 275(1), 207–227.
- 665 Sillanpää, I., Ganushkina, N. Y., Dubyagin, S., & Rodriguez, J. (2017). Electron
666 fluxes at geostationary orbit from goes maged data. *Space Weather*, 15(12), 1602–
667 1614.
- 668 Spearman, C. (1961). *The proof and measurement of association between two things*.
669 Appleton-Century-Crofts.
- 670 St Cyr, O., Kaiser, M., Meyer-Vernet, N., Howard, R., Harrison, R., Bale, S., ...
671 others (2009). Stereo secchi and s/waves observations of spacecraft debris caused
672 by micron-size interplanetary dust impacts. *Solar Physics*, 256(1), 475–488.
- 673 Wanliss, J. A., & Showalter, K. M. (2006). High-resolution global storm index: Dst
674 versus sym-h. *Journal of Geophysical Research: Space Physics*, 111(A2).
- 675 Whitman, K., Egeland, R., Richardson, I. G., Allison, C., Quinn, P., Barzilla, J.,
676 ... others (2022). Review of solar energetic particle models. *Advances in Space*
677 *Research*.
- 678 Woods, T., Eparvier, F., Hock, R., Jones, A., Woodraska, D., Judge, D., ... others
679 (2010). Extreme ultraviolet variability experiment (eve) on the solar dynamics ob-
680 servatory (sdo): Overview of science objectives, instrument design, data products,
681 and model developments. *The solar dynamics observatory*, 115–143.
- 682 Young, P., Doschek, G., Warren, H., & Hara, H. (2013). Properties of a solar flare
683 kernel observed by hinode and sdo. *The Astrophysical Journal*, 766(2), 127.
- 684 Young, P., & Muglach, K. (2014). Solar dynamics observatory and hinode observa-
685 tions of a blowout jet in a coronal hole. *Solar Physics*, 289(9), 3313–3329.
- 686 Young, P. R., Viall, N. M., Kirk, M. S., Mason, E. I., & Chitta, L. P. (2021). An
687 analysis of spikes in atmospheric imaging assembly (aia) data. *Solar Physics*,

